Magnitude Limits of Subduction Zone Earthquakes

Citation	Rong, Y., Jackson, D. D., Magistrale, H., Goldfinger, C. (2014). Magnitude Limits of Subduction Zone Earthquakes. Bulletin of the Seismological Society of America, 104(5), 2359-2377. doi:10.1785/0120130287
DOI	10.1785/0120130287
Publisher	Seismological Society of America
Version	Version of Record
Terms of Use	http://cdss.library.oregonstate.edu/sa-termsofuse

THE SEISMOLOGICAL SOCIETY OF AMERICA
400 Evelyn Ave., Suite 201
Albany, CA 94706-1375
(510) 525-5474; FAX (510) 525-7204
www.seismosoc.org

Bulletin of the Seismological Society of America, Vol. 104, No. 5, pp. 2359–2377, October 2014, doi: 10.1785/0120130287

Magnitude Limits of Subduction Zone Earthquakes

by Yufang Rong, David D. Jackson, Harold Magistrale, and Chris Goldfinger

Abstract Maximum earthquake magnitude (m_x) is a critical parameter in seismic hazard and risk analysis. However, some recent large earthquakes have shown that most of the existing methods for estimating m_x are inadequate. Moreover, m_x itself is ill-defined because its meaning largely depends on the context, and it usually cannot be inferred using existing data without associating it with a time interval. In this study, we use probable maximum earthquake magnitude within a time period of interest, $m_p(T)$, to replace m_x. The term $m_p(T)$ contains not only the information of magnitude limit but also the occurrence rate of the extreme events. We estimate $m_p(T)$ for circum-Pacific subduction zones using tapered Gutenberg–Richter (TGR) distributions. The estimation of the two TGR parameters, β-value and corner magnitude (m_c), is performed using the maximum-likelihood method with the constraint from tectonic moment rate. To populate the TGR, the rates of smaller earthquakes are needed. We apply the Whole Earth model, a high-resolution global estimate of the rate of $m \geq 5$ earthquakes, to estimate these rates. The uncertainties of $m_p(T)$ are calculated using Monte-Carlo simulation. Our results show that most of the circum-Pacific subduction zones can generate $m \geq 8.5$ earthquakes over a 250-year interval, $m \geq 8.8$ earthquakes over a 500-year interval, and $m \geq 9.0$ earthquakes over a 10,000-year interval. For the Cascadia subduction zone, we include the 10,000-year paleoseismic record based on turbidite studies to supplement the limited instrumental earthquake data. Our results show that over a 500-year period, $m \geq 8.8$ earthquakes are expected in this zone; over a 1000-year period, $m \geq 9.0$ earthquakes are expected; and over a 10,000-year period, $m \geq 9.3$ earthquakes are expected.

Introduction

Almost all probabilistic seismic-hazard analyses use earthquake magnitude–frequency distributions to characterize earthquakes in a region. In the widely used truncated Gutenberg–Richter (GR) distribution, maximum earthquake magnitude, m_x, is the hard cutoff magnitude: earthquakes larger than m_x will not be considered in the seismic-hazard analysis. Unfortunately, due to the short time span of historical earthquake catalogs, it is difficult to obtain a reliable estimation of m_x.

Both the devastating 2004 m 9.1 Sumatra–Andaman and the 2011 m 9.0 Tohoku earthquakes surprised geoscientists. Most of the prior hazard estimates of the Tohoku region limited the maximum magnitude to below 8.5 (Ruff and Kanamori, 1980; Earthquake Research Committee, 2005). The largest known historical earthquake in the region before the 2011 earthquake was the A.D. 869 Jogan earthquake, estimated to have a magnitude of 8.3–8.4 based on the analysis of tsunami deposits (Minoura *et al.*, 2001; Sugawara *et al.*, 2012). In the Sumatra region, earthquakes of about magnitude 8 were not unexpected using the empirical relationship between largest earthquake magnitude, oceanic lithosphere age, and convergence rate by Ruff and Kanamori (1980) and from the available earthquake history, but magnitude 9+ events were unexpected. At least four factors contributed to the underestimation of m_x: (1) no such large earthquakes had been recorded in the regions; (2) an *ad hoc* fault segmentation model was overweighted in estimating m_x; (3) convergence is nearly fault parallel along the northern Sumatra subduction zone, that was thought to limit strain accumulation on the megathrust; and (4) the proposed empirical relationship between the largest earthquake magnitude, lithosphere age, and subduction rate gives only magnitude 8+ earthquakes (Ruff and Kanamori, 1980; Kanamori, 2006; Stein and Okal, 2011). These factors are key issues existing in some methods for estimating m_x. Historical earthquake catalogs are too short, and paleoseismic data are far from complete. The common practice of adding a quarter- or half-unit of magnitude to the largest recorded magnitude (e.g., Gaull *et al.*, 1990; Musson, 2000; Vilanova and Fonseca, 2007; Secanell *et al.*, 2008) is arbitrary and insufficient to capture m_x. Another common practice is to use fault length–magnitude scaling relationships. When this method is used to estimate m_x, one of the assumptions is that the two ends of a fault or fault segment are known, and earthquakes will not rupture through the ends and jump to

another fault or segment. The ends of a fault are usually determined from fault traces on a map, subject to errors and incompleteness. Moreover, multiple segments can be ruptured by a single event. The 2011 m 9.0 Tohoku earthquake ruptured all the proposed subduction segments in the Tohoku area, although evidence for the segmentation was weak. The 2007 m 8.1 Solomon Islands earthquake ruptured through the triple junction of the Australia, Pacific, and Woodlark plates, which was thought to be a substantial geologic boundary (Furlong *et al.*, 2009). The 2002 m 7.9 Denali fault earthquake started with vertical motion on a previously unknown thrust fault, the Susitna Glacier fault, continued on the Denali fault, and jumped onto the Totschunda fault. Stein and Okal (2011) used additional and more accurate data of lithosphere age and convergence rate to examine the relationship by Ruff and Kanamori (1980) and found that the seemingly compelling pattern between magnitude, oceanic lithosphere age, and convergence rate disappeared. McCaffrey (2008) and Goldfinger, Ikeda, *et al.* (2013) both suggest for different reasons that larger earthquakes than presently known may well characterize many subduction zones, but records are too short and incomplete to have revealed this conjecture.

The parameter m_x is used not only in earthquake magnitude–frequency distributions by seismologists but also in engineering design by earthquake engineers. In practice, different kinds of maximum earthquakes have been employed such as maximum possible earthquake, maximum credible earthquake, maximum expectable, or maximum probable earthquake (Reiter, 1990). Thus, the meaning of m_x largely depends on the context. In fact, without specifying a time interval over which it is valid, the m_x itself is ill-defined (Pisarenko *et al.*, 2008). With an absolute m_x, it is difficult to argue why an earthquake with a little bit larger magnitude is not possible. In addition, m_x is usually not inferable from the instrumental and historical earthquake data, because the record is too short for great earthquakes. Holschneider *et al.* (2011) suggested using the maximum expected magnitude in a given time interval T to replace the maximum possible magnitude, because confidence intervals of m_x diverge for most of the cases. Zöller *et al.* (2013) presented a statistical model for the estimation of the maximum earthquake magnitude to occur in a time interval T in the future. In line with the above studies, we use the terminology $m_p(T)$, probable maximum magnitude within period of interest T, in this study. The $m_p(T)$ contains not only the information of magnitude limit but also the occurrence rate of the extreme events. Instead of solving for the absolute m_x, we estimate $m_p(T)$ for each of the circum-Pacific subduction zones. The largest expected earthquake in any time period is subject to natural variability; we take $m_p(T)$ to represent the median of a probability density distribution, which we estimate along with its uncertainty.

We use several different measures of large earthquake magnitudes, distinguishable in the text only by some tiny subscripts, but with their meanings differing significantly. Table 1 summarizes the measures.

Estimating Probable Maximum Magnitude

Magnitude–Frequency Distributions

The GR relationship states that, in a given region and for a given period of time, the cumulative number of earthquakes can be represented by

$$\log_{10} N = a - bm, \tag{1}$$

in which m is the magnitude, N is the number of events with magnitude equal to or larger than m, and a and b are constants. This equation describes the relative ratio of large-to-small earthquakes. The GR relationship is one of the most important scaling relationships in seismology.

The seismic moment (M) of an earthquake is a measure of its total displacement, integrated over area, and it is proportional to the energy released by the earthquake. There is a close relationship between m and M (Hanks and Kanamori, 1979):

$$M = 10^{1.5m+C}, \tag{2}$$

in which M is in newton meters (N·m). Here we take $C = 9.0$, although published values range from 9.0 to 9.1. Thus, reported magnitudes may differ from one publication to another, but the seismic moments should be identical. Seismic moment can also be related to faulting parameters: for a simple idealized earthquake with uniform slip d over a fault plane with area S in a uniform medium with rigidity μ, the seismic moment is

$$M = \mu S d. \tag{3}$$

Seismic moment is a very useful concept because it is additive: a collection of earthquakes produces a total seismic moment equal to the sum of the individual moments. Furthermore, over a long time, the total moment on a fault or plate boundary can be estimated from the product of its locked area and total slip. This moment, which we refer to as the tectonic moment, should be equal to the sum of seismic moments of the earthquakes accommodating the fault or plate motion over a long (generally very long) time. Application of this simple equality is of course complicated by several factors, including imperfect and poorly known coupling, poorly characterized coupled area, and uncertain value of μ.

Because each earthquake contributes a magnitude-dependent seismic moment, the distribution of earthquake sizes implies a distribution of tectonic moment release. Measured tectonic moment might be explained by a few very large earthquakes, or many more small ones, or more realistically by a distribution of large and small ones. For this purpose, the GR relationship is inadequate: it implies an exponentially decreasing rate of large earthquakes, but their seismic moments increase exponentially, with the result that the implied total seismic moment rate would be infinite. To overcome this paradox, novel models have been proposed to

address the deviations from the GR relationship at the tail of the magnitude–frequency distributions and the issue of infinite seismic energy. Unfortunately, all the models suffer from large statistical uncertainty due to the insufficient number of observed large earthquakes.

A simple modification to the GR relationship is to truncate it, by setting either the density (earthquakes per magnitude unit) or cumulative rate abruptly to zero. The truncated GR has been widely used in probabilistic seismic-hazard analyses such as the national seismic-hazard maps of the United States (Frankel *et al.*, 1996, 2002; Petersen *et al.*, 2008).

Another modification of the GR relationship is the tapered Gutenberg–Richter (TGR) distribution (Kagan, 1997; Kagan and Schoenberg, 2001; Bird and Kagan, 2004). The TGR relation is best expressed in seismic moment, M, instead of magnitude. It has an exponential taper applied to the number of events of large seismic moment. The TGR magnitude distribution is

$$F(M) = \left(\frac{M_t}{M}\right)^{\beta} \exp\left(\frac{M_t - M}{M_c}\right) \quad \text{for } M_t \le M < \infty, \quad (4)$$

(Kagan, 2002a) in which β is the index parameter of the distribution, and $\beta = 2/3b$. M_c is called corner moment (the corresponding magnitude is called corner magnitude, m_c; Table 1), which controls the distribution in the upper ranges of M. M_t is a threshold moment (the corresponding magnitude is threshold magnitude, m_t) above which the catalog is assumed to be complete. $F(M)$ is the rate of earthquake moment larger than M, normalized to a cumulative rate of 1 at the threshold magnitude m_t. When $M_c \to \infty$, the TGR relationship is equivalent to the GR relationship.

Both truncated GR and TGR have two parameters: a b-value and a parameter describing a modification of the simple GR law for very large earthquakes, and both distributions ensure a finite seismic moment flux for a region. Bell *et al.* (2013) showed that a preferred model of global earthquakes converges to a TGR distribution. However, Zöller (2013) demonstrated that, statistically, the truncated and TGR distributions performed equally well for the global seismicity. Because a sharp cutoff at the tail of the truncated GR distribution contradicts the known behavior of dissipative physical dynamic systems that require a smooth transition, the TGR distribution is more physically defensible using observed seismicity and seismic moment balances (Kagan, 2002a; Bird and Kagan, 2004; Pisarenko and Sornette, 2004).

Approach

To solve for the probable maximum magnitude, $m_p(T)$, the basic steps in our analysis are to:

1. identify polygons describing major subduction zones where we will estimate the probabilities of large earthquakes;
2. choose the lower threshold magnitude m_t, at or above which the catalog is complete;
3. estimate the threshold rate, that is, the rate of magnitude m_t and larger earthquakes within each polygon; and
4. construct earthquake magnitude distributions and estimate the probability of great earthquakes within each polygon from the threshold rate and the appropriate magnitude distribution.

Table 1
A Glossary of Large Magnitude Parameters

Measure	Meaning
m_x	Absolute maximum; assumed maximum possible earthquake size for a given region.
m_h	Historic maximum; magnitude of largest earthquake observed or inferred to have occurred in the region.
m_c	Corner magnitude; a parameter in the tapered Gutenberg–Richter distribution, indicating the magnitude at which the rate is $1/e$ times that implied by a simple Gutenberg–Richter relationship.
$m_p(T)$	Probable maximum magnitude expected in time interval T.

For the first step, we adopt polygons (F-E zones) defined by Flinn and Engdahl (1965) and Flinn *et al.* (1974) (Fig. 1). We chose them because they define the subduction zones reasonably well, and most important, they were defined before the start of the Global Centroid Moment Tensor (CMT) (Ekström *et al.*, 2005) earthquake catalog that we use for many of our statistical tests. Thus, they are independent of the test earthquakes, avoiding the potential selection bias that could occur if the zones were drawn to include or exclude individual earthquakes. F-E zone 3 covers only the southern Cascadia subduction zone (CSZ); we will deal with this subduction zone separately.

For the earthquake magnitude completeness and threshold rate estimates of steps 2 and 3, we rely on the Whole Earth model study by Kagan and Jackson (2012), which is a smoothed seismicity model for the world. Kagan and Jackson (2012) used the U.S. Geological Survey (USGS) Preliminary Determinations of Epicenters (PDE) earthquake catalog (Sipkin *et al.*, 2000), which is complete at $m \ge 5$ since 1969, for earthquake locations. For magnitudes, they generally used the moment magnitude. Moment magnitudes were first reported consistently in the Global CMT catalog beginning in about 1977, but now the PDE catalog includes moment magnitudes for most earthquakes over magnitude 5.0. In some cases, locations were reported in the PDE catalog, but moment magnitudes were reported only in the Global CMT catalog. In those cases, Kagan and Jackson used the more accurate locations from the PDE and the more accurate moments from the Global CMT.

For step 4, we construct an earthquake magnitude–frequency distribution for each F-E zone. We choose the TGR distribution because it provides the needed limit on the long-term moment rate, it fits several catalogs well with many sufficiently large earthquakes, and it affords relatively easy computation. After completing the four steps, $m_p(T)$ can be

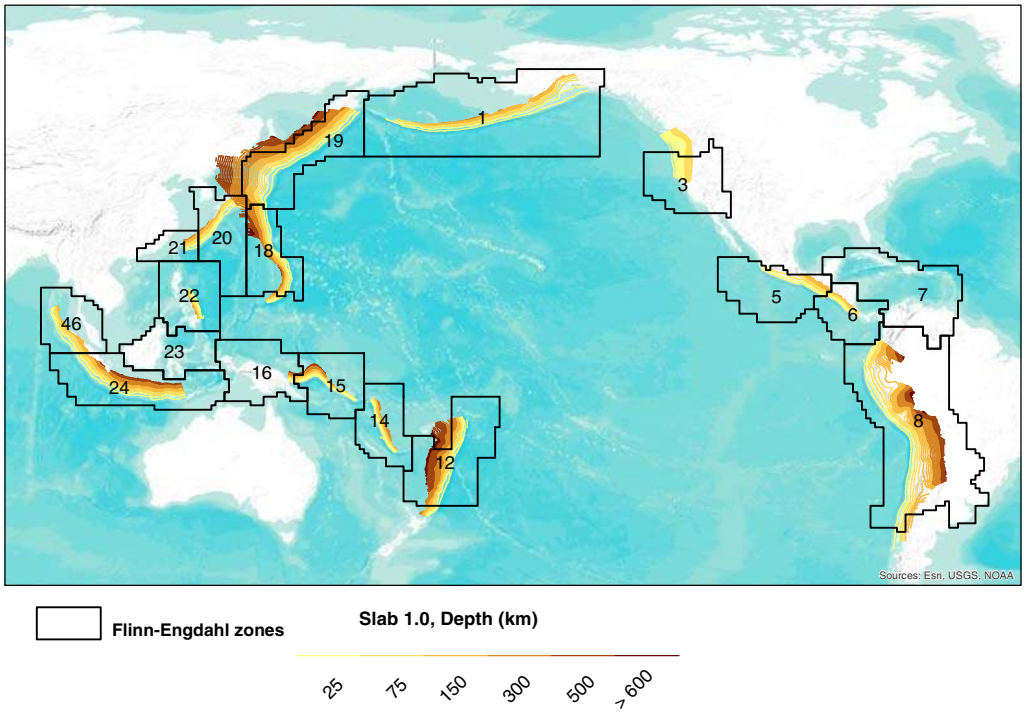

Figure 1. Subduction regions around the Pacific Ocean defined by Flinn–Engdahl (F-E) (Flinn and Engdahl, 1965; Flinn *et al.*, 1974) and Slab 1.0 (Hayes *et al.*, 2012). F-E zones (black polygons) are: 1, Alaska-Aleutian arc; 3, Oregon, California, and Nevada; 5, Mexico-Guatemala; 6, Central America; 7, Caribbean Loop; 8, Andean South America; 12, Kermadec-Tonga-Samoa; 14, New Hebrides Islands; 15, Bismarck-Solomon Islands; 16, New Guinea; 18, Guam-Japan; 19, Japan-Kamchatka; 20, Japan-Ryukyu Islands; 21, Taiwan; 22, Philippines; 23, Borneo-Celebes; 24, Sunda arc; 46, Andaman Island. The Slab 1.0 model is represented by light (shallow) to dark (deep) depth-to-slab contour lines. The color version of this figure is available only in the electronic edition.

read from the TGR curve: $m_p(T)$ is the magnitude corresponding to $1/T$ occurrence rate on the curve.

Theoretically, the TGR parameters β and M_c (or m_c) can be estimated by the maximum-likelihood method from earthquake data alone, if the catalog has a sufficient number of large earthquakes. The maximum-likelihood method requires computation of a log-likelihood function l, which is the natural logarithm of the likelihood that the given catalog would be observed if the current trial values of β and M_c were correct, under the constraint that the number of earthquakes in the catalog with $M_i > M_t$, N, is fixed. For the TGR distribution,

$$l = N\beta \ln(M_t) + \frac{1}{M_c}\left(NM_t - \sum_{i=1}^{N} M_i\right) - \beta \sum_{i=1}^{N} \ln(M_i) + \sum_{i=1}^{N} \ln\left(\frac{\beta}{M_i} + \frac{1}{M_c}\right) \quad (5)$$

(Kagan, 2002a; Bird and Kagan, 2004). The maximum-likelihood estimates of β and M_c are associated with l_{max}, the highest value of l. The maximum-likelihood estimates of β and M_c (or b and m_c) have a slight negative bias. From 1000 simulations, we estimate that, with 100 events above the magnitude m_c-2, the estimated m_c and b-values are (m_c−0.16) ±0.32 and (b−0.02) ±0.10. With 200 events, typical of most of our subduction zone catalogs, the values are (m_c−0.09) ±0.25 and (b−0.006) ±0.076. Given the uncertainties, we interpret results using the 95% confidence limits derived from contours of the likelihood function. For large N, the quantity $w \equiv 2(l_{max} - l)$ is distributed approximately as a chi-square variable with two degrees of freedom, implying elliptical contours as generally observed. Then the 95% confidence limit for w is about 6 (Bird and Kagan, 2004), and $l_{max} - 3$ serves as a useful measure of the 95% confidence region. Assuming a uniform constant prior distribution and that the likelihood function can be normalized, the posterior joint probability density function of the two parameters is by Bayes' rule a normalized version of the likelihood function (Zöller *et al.*, 2013). Jackson and Matsu'ura (1985) showed by simulation that confidence limits estimated from the likelihood function are close to those from the posterior distribution if the prior distribution is nearly uniform within the inferred confidence region, and the product of likelihood function and prior distribution can be normalized. If the likelihood function is indeed nearly chi-square, then the 95% confidence limits are approximated well by ($l_{max} - 3$). However, that contour may not close at a reasonable value of the corner moment if the catalog is too deficient in large earthquakes. As shown below, inclusion of additional data such as tectonic moment rate may be valuable for placing a meaningful upper confidence bound on m_c.

Otherwise, only the assumed prior distribution controls the confidence limits of m_c.

In another method, we use the moment rate conservation principle to constrain M_c (or m_c). That principle states that a certain part of tectonic deformation is released by the cumulative effects of earthquakes. The seismic moment rate, $\dot{M}_s$, can be estimated either by summing up moments of known earthquakes or by integrating theoretical moment–frequency relations. The former method may yield very unstable estimates because of the relatively short instrumental earthquake catalog and relatively long recurrence of great earthquakes. The latter method depends on the estimation of the parameters in the theoretical relations. Using a TGR relation, the estimation of $\dot{M}_s$ depends on three variables: r_t, the rate of earthquakes in the region larger than the threshold magnitude, the β-value, and M_c. For an active subduction zone, quite stable estimates of r_t and β can be obtained from catalog statistics.

The tectonic moment rate can be estimated by

$$\dot{M}_T = \chi \mu W L \bar{u}, \tag{6}$$

in which χ is the seismic coupling coefficient, μ is the rigidity, W is the down-dip width of the seismogenic zone, L is the length of a fault, and $\bar{u}$ is the plate velocity. The parameters χ, W, and μ are usually not well determined and are subject to large uncertainties.

The seismic coupling coefficient represents the fraction of plate tectonic motion within the lock zone released by earthquakes. Other strain release processes include creep (as afterslip or in the velocity strengthening zone below the locked zone) and slow-slip events, with or without seismic tremors (Schwartz and Rokosky, 2007). Slow-slip events usually occur at the transition between the velocity weakening and strengthening zones (Cascadia, Mexico, New Zealand, Alaska) but may also occur within the velocity weakening zone (Japan, Costa Rica; Schwartz and Rokosky, 2007). In Cascadia, 45%–65% of the plate convergence rate is accommodated by slow-slip events below the locked zone, however, any potential slow-slip strain release in the locked zone is too small to be detected by Global Positioning System (GPS; Wech *et al.*, 2009; Gomberg *et al.*, 2010). It is difficult to quantify the fraction of tectonic moment released by aseismic processes in the locked zone; for subduction zones, the coupling coefficient is usually between 0.5 and 1.0 (Scholz and Campos, 2012).

The seismogenic zone down-dip width is defined as the distance between the up-dip limit near the trench and the down-dip limit (i.e., the locked part of a subduction zone) along the subduction slab, and typical values are about 60–170 km (Hayes *et al.*, 2012). Typical rigidity values used in the calculation are 30 (McCaffrey, 2008) and 49 GPa (Kagan and Jackson, 2013). The tectonic moment rate is usually estimated from geodetic strain rate maps (Bird and Kagan, 2004; Bird and Liu, 2007; Bird *et al.*, 2010).

Kagan and Jackson (2013) calculated the β-values for the F-E subduction zones using the maximum-likelihood method and the Global CMT catalog from 1977 to 2010. They also calculated tectonic moment rates for the zones based on the geodetic strain rate map by Kreemer *et al.* (2003) using the method described in Bird and Liu (2007) and Bird *et al.* (2010). They used $W = 104$ km, $\mu = 49$ GPa, and $\chi = 0.5$. Alternative values of W, μ, and χ with $W = 100$ km, $\mu = 30$ GPa, and $\chi = 0.85$ (e.g., Scholz and Campos, 2012) produce the same value of $\dot{M}_T$ (see equation 6) as those of Kagan and Jackson (2013). The coupling coefficient may be time dependent. Here, we use a constant value and consider it a long-term average. Kagan and Jackson (2013) estimated the corner magnitude for a theoretical magnitude distribution referred to as the gamma magnitude distribution in Kagan (2002a,b). The gamma magnitude distribution is closely related to the TGR distribution we use here, but it is slightly different and the meaning of corner magnitude is different for the two distributions.

Using the seismic moment conservation principle, the TGR M_c can be estimated as (Kagan, 2002b)

$$M_c \simeq \left[\frac{\chi \dot{M}_T (1-\beta)}{\alpha_t M_t^{\beta} \Gamma(2-\beta)}\right]^{1/(1-\beta)}, \tag{7}$$

in which α_t is the seismic activity level (occurrence rate) for earthquakes with moment M_t and greater, and Γ is the gamma function.

In this study, for all the subduction zones except Cascadia, we adopted the β-values and tectonic moment rates in Kagan and Jackson (2013), and derived m_c and its uncertainty for the TGR distribution, constrained by the observed tectonic moment rate. The results are listed in Table 2. We present two sets of m_c and β-values: one m_c set is derived using zone-specific β-value for each region, and the other is derived using the generic β-value of 0.65 for all the F-E zones. The specific β-value for an F-E zone is the value derived using the earthquake data within that zone. The generic β-value is the value derived using the earthquake data in all the zones. The generic β-value is close to a b-value of 1.0. When the specific β-values are used, m_c varies significantly between zones. When the generic β-value is used, the m_c values are similar for all the zones. The uncertainties of TGR m_c are very similar to those for the gamma distribution used in Kagan and Jackson (2013). The distinction between this study and Kagan and Jackson (2013) is that (1) we derived the m_c values for TGR distribution instead of gamma distribution; (2) we integrated paleoseismic data into the Cascadia analysis; and (3) we estimated $m_p(T)$ values, presented in the Results section.

Cascadia Subduction Zone

Magnitude of Cascadia Earthquakes

The CSZ is formed by the subduction of the oceanic Juan de Fuca and Gorda Plates beneath the North America Plate off the coast of northern California, Oregon, Washington, and Vancouver Island. The earthquake potential of the

Table 2
Corner Magnitude (m_c), β-value, and Standard Deviations (σ) of Each of the F-E Subduction Zones Based on TGR Distribution

F-E Zone Number	Name	N*	Zone-Specific β-Value				Generic β-Value	
			β	σ_β	m_c	σ_{m_c}	β	m_c
1	Alaska-Aleutian arc	280	0.65	0.04	9.01	0.28		9.01
5	Mexico-Guatemala	164	0.60	0.06	8.55	0.29		8.82
6	Central America	161	0.68	0.06	9.08	0.29		8.88
7	Caribbean Loop	59	0.62	0.09	8.81	0.31		8.99
8	Andean South America	286	0.57	0.04	8.89	0.28		9.42
12	Kermadec-Tonga-Samoa	439	0.80	0.04	10.14	0.28		8.77
14	New Hebrides Islands	424	0.59	0.03	8.32	0.28		8.62
15	Bismarck-Solomon Islands	448	0.60	0.03	8.35	0.28		8.59
16	New Guinea	266	0.66	0.05	9.56	0.28	0.65	9.48
18	Guam-Japan	88	0.86	0.10	13.05	0.30		9.50
19	Japan-Kamchatka	425	0.62	0.04	8.89	0.28		9.09
20	S.E. Japan-Ryukyu Islands	57	0.62	0.10	9.25	0.31		9.47
21	Taiwan	110	0.64	0.07	8.73	0.29		8.79
22	Philippines	244	0.68	0.05	9.02	0.28		8.82
23	Borneo-Celebes	266	0.68	0.05	9.09	0.28		8.89
24	Sunda arc	278	0.65	0.04	9.22	0.28		9.22
46	Andaman Island Sumatra	143	0.71	0.07	9.50	0.29		9.03
	All (1977–2010)	4217	0.65	0.01	9.02	0.27		9.02

*Number of $m \geq 5.8$ earthquakes in the Global CMT catalog from 1977 to 2010.

CSZ has been discussed by Atwater (1987), Savage and Lisowski (1991), Mitchell *et al.* (1994), Atwater *et al.* (1995), Hyndman and Wang (1995), Satake *et al.* (1996, 2003), McCaffrey *et al.* (2000), Mazzotti *et al.* (2003), and Nelson *et al.* (2006). Despite the presence of abundant paleoseismic evidence for rapid coastal subsidence and tsunamis, the Cascadia plate boundary remains seismically the quietest of all circum-Pacific subduction zones, with only one significant interplate thrust event (the 1992 m 7.1 Cape Mendocino earthquake) ever recorded instrumentally (Oppenheimer *et al.*, 1993). Fortunately, strong shaking caused by the great subduction zone earthquakes can trigger turbidity currents, which leave deposits in marine sediments. As a result, an ~10,000-year turbidite record has been developed during the investigation of the turbidite system along the CSZ (Goldfinger *et al.*, 2012). The turbidite and onshore paleoseismic records can be used to reconstruct the large earthquake history in the region.

Goldfinger *et al.* (2012) interpreted the turbidite data and suggested four types of earthquake rupture along the CSZ during the past 10,000 years (Fig. 2 and Table 3): (1) 19–20 full-margin or nearly full-margin ruptures (section A); (2) three or four ruptures of the southern 50%–70% of the margin (section B); (3) 10–12 southern ruptures from central Oregon southward (section C); and (4) 7–8 southern Oregon/northern California events with the possibility of unresolved events (section D). Regarding the accuracy of the rupture extents shown in Figure 2, Goldfinger *et al.* (2007) concluded the maximum distance from an earthquake rupture to a triggered turbidity current is likely less than 90 km for full-margin Cascadia events and less for smaller events. Hence, it is reasonable to use the distance between offshore core sites containing turbidites from the same event (or correlation length) to represent the approximate length of the ruptures. Goldfinger, Morey, *et al.* (2013) reiterate and slightly revise the southern rupture segment conclusions using additional cores and high-resolution seismic reflection data.

The turbidite data do not contain direct indicators of earthquake magnitude. However, some indirect indicators can be used for that estimate. First, Goldfinger *et al.* (2012) noted strong relations between the correlated rupture length and turbidite thickness and turbidite mass, and interpreted those to indicate that longer ruptures are associated with greater shaking. Second, there is a correlation between turbidite mass per event at several widely separated sites. This indicates that, at least for the Holocene and the selected sites, there is a consistent relationship between the evidence for shaking along strike for many of the events. Goldfinger *et al.* (2012) estimated the magnitude of the events based on these observations. They used interevent time following each event to calculate average slip, an assumed coupling coefficient of 1.0 as strongly suggested by the geodetic data (Hyndman and Wang, 1995; McCaffrey *et al.*, 2000, 2013; Wang *et al.*, 2003; Scholz and Campos, 2012), and rupture lengths based on the distances between correlated sites. The rupture widths were based on geophysical and geodetic estimates, and were assumed to be 83, 60, 50, and 40 km for four types of rupture, respectively, assuming reduced width for smaller ruptures, except that 55 km is used for events T2, T12, T17, and T17a to account for their relatively thin turbidite beds and/or short interevent time. Table 3 lists the parameters and the estimated moment magnitudes.

The estimated magnitudes by Goldfinger *et al.* (2012) are uncertain considering that the strain accumulation and slip for each event were unknown (Goldfinger *et al.*, 2012).

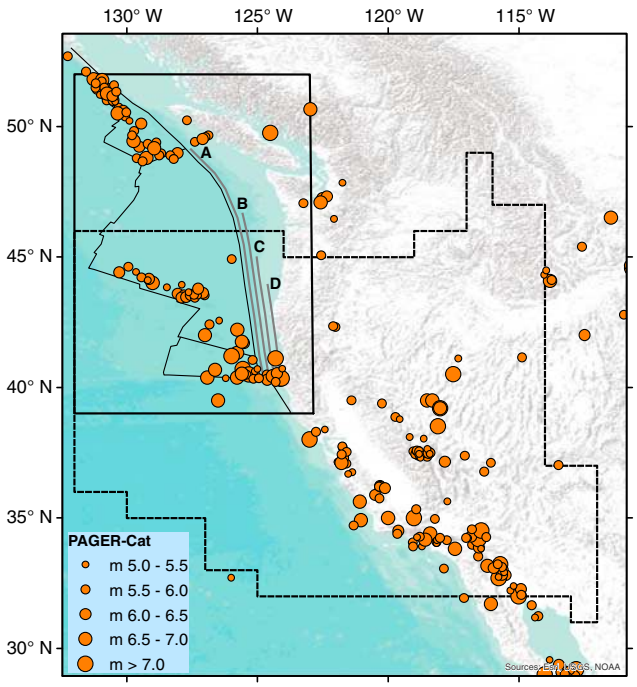

Figure 2. Original Flinn–Engdahl zone 3 (the polygon defined by black dashed lines) and the redefined Cascadia region (the rectangular box defined by thick solid black line). Thin black lines show the plate boundaries in the Cascadia region. Circles are historical earthquakes in the PAGER-CAT catalog (Allen *et al.*, 2009) since 1900. The four gray lines labeled from A to D represent the four rupture sections listed in Table 3. Note that the four sections are intentionally shifted from the plate boundary so that they can be seen on the map. The color version of this figure is available only in the electronic edition.

We consider three alternate sets of magnitudes based on different assumptions. In the first, we use the method of Goldfinger *et al.* (2012) but with different rupture widths. The rupture widths used by Goldfinger *et al.* (2012) were inferred from published thermal models (Hyndman and Wang, 1995; Flück *et al.*, 1997), GPS-based models (McCaffrey *et al.*, 2007), and the structural transition from contraction to extension (Priest *et al.*, 2009). However, episodic tremor and slip (ETS) data have been interpreted to suggest that future coseismic rupture might extend to 25 km depth, or ~60 km inland of the Pacific coast, rather than stopping offshore at 15 km depth (Chapman and Melbourne, 2009). In fact, almost all of the $m \geq 8.8$ earthquakes along other subduction zones ruptured more than a 100 km down-dip width (Strasser *et al.*, 2010). The rupture width of the 2011 m 9.0 Tohoku earthquake was about 200 km, although the rupture length was only about 450 km (Yoshida *et al.*, 2011). The rupture width of the 2011 Chile m 8.8 earthquake was estimated to be larger than 140 km (Wang *et al.*, 2012, and references therein). Kagan (2002c) investigated the distribution of aftershock zones for large earthquakes. He found that all earthquakes show the same magnitude-rupture scaling and that earthquake geometrical focal zone parameters are self-similar. Using the scaling relationship and the self-similarity characteristics proposed by Kagan (2002c), the CSZ rupture lengths of 1000, 660, 444, and 222 km correspond to rupture widths of 126, 84, 56, and 28 km, respectively. By replacing the rupture widths in Table 3 with these values, we obtain a set of alternative magnitudes (the column m_{alt1} in Table 3).

The columns m and m_{alt1} in Table 3 were estimated based on a simple time-predicable model, which is essentially the seismic gap theory, and assumes that the seismic moment in a given megaquake is accumulated only since the previous one. Rong *et al.* (2003) showed that the seismic gap model does not work well globally. Goldfinger, Ikeda, *et al.* (2013) estimated the energy state of the 19 full-margin rupture events using the recurrence time between events to represent energy gain and the turbidite mass per event to represent energy loss (mass per event was estimated at several core sites based on core density data, averaged and given separately for each event). They concluded the Cascadia earthquakes followed neither a time-predicable nor a slip-predicable model: instead, they propose a long-term cycling of energy storage and release. For the 19 full-margin rupture events, the turbidite mass and thickness vary considerably from event to event at each site but are relatively consistent for the same event from site to site (Goldfinger *et al.*, 2012, Goldfinger, Ikeda, *et al.*, 2013). Because of this consistency for individual events along the margin, and despite the obvious simplification involved, Goldfinger, Ikeda, *et al.* (2013) inferred that turbidite mass can be considered a crude proxy for seismic moment or intensity of ground shaking at offshore sites for at least the 19 full-margin rupture events.

Accordingly, we propose another way to estimate magnitudes of the full-margin rupture events. We use the 1700 earthquake as a reference and assume that it has a magnitude of 9.0 (Satake *et al.*, 2003), then the seismic moment of the ith event, $M(i)$, can be estimated by

$$M(i) = M(1) \times [\mathrm{mass}(i)/\mathrm{mass}(1)]^{x}, \tag{8}$$

in which $M(1)$ and mass(1) are the seismic moment and turbidite mass (the average of four sites) of the 1700 earthquake, and mass(i) is the turbidite mass (the average of five sites) of the ith event. We vary x and find that the total seismic moment rate is about in the range of the tectonic moment rate estimated using the Global Strain Rate Model (Kreemer *et al.*, 2003) when x is between 0.5 and 1.0. Thus, we obtain another two sets of magnitudes by assuming $x = 0.5$ and $x = 1.0$ (the columns m_{alt2} and m_{alt3} in Table 3, respectively). For the partial-margin rupture events, we cannot use this method to infer magnitudes because a reliable correlation of turbidite mass between different sites has not been demonstrated. Therefore, for those partial margin rupture events, we use the magnitudes determined by the first alternative method. The estimated alternate magnitudes are subject to large uncertainties; however, they represent some reasonable range of the magnitudes of great CSZ events.

Table 3
Estimated Earthquake Magnitudes of the Turbidite Events

Turbidite Number	Mean Age*	Northern Margin Following Interval (years)*	Southern Margin Following Interval (years)*	Section Name*	Rupture Length (km)*	Rupture Width (km)*	m*	m_{alt1}†	m_{alt2}†	m_{alt3}†
1	250			A	1000	83	9.00	9.15	9.00	9.00
2	482	232	232	A	1000	55	8.70	8.97	8.95	8.89
2a	550		57	D	222	40	8.19	8.56	7.70	7.70
3	798	305	248	A	1000	83	8.87	9.02	9.05	9.10
3a	1077		279	C	444	50	8.34	8.68	8.55	8.55
4	1243	446	167	A	1000	83	8.90	9.05	9.03	9.06
4a	1429		186	C	444	50	8.25	8.33	8.43	8.43
5	1554	311	125	A	1000	83	8.80	8.95	9.05	9.11
5a	1820		266	C	444	50	8.41	8.61	8.54	8.54
5b	2036		216	B	660	60	8.66	7.96	8.71	8.71
5c	2323		286	C	444	50	8.41	8.28	8.56	8.56
6	2536	982	213	A	1000	83	9.09	9.24	9.07	9.14
6a	2730		194	D	222	40	8.24	8.19	8.04	8.04
7	3028	492	298	A	1000	83	8.97	9.12	9.09	9.18
7a	3157		129	D	222	40	8.23	8.16	7.92	7.92
8	3443	415	286	A	1000	83	8.94	9.09	9.08	9.16
8a	3599		442	B	660	60	8.67	8.00	8.61	8.61
8b	3890		447	D	222	40	8.15	7.70	8.16	8.16
9	4108	665	218	A	1000	83	9.01	9.16	9.04	9.08
9a	4438		548	B	660	60	8.35	8.55	8.83	8.83
9b	4535		426	D	222	40	8.17	8.43	7.84	7.84
10	4770	661	235	A	1000	83	9.01	9.09	9.05	9.10
10a	5062		292	C	444	50	8.39	8.54	8.56	8.56
10b	5260		198	B	660	60	8.43	8.71	8.68	8.68
10c	5390		130	C	444	50	8.55	8.56	8.33	8.33
10d	5735		344	C	444	50	7.9	8.04	8.61	8.61
10f	5772		37	C	444	50	8.37	7.92	7.96	7.96
11	5959	1189	187	A	1000	83	9.13	9.28	9.19	9.38
12	6466	508	508	A	1000	55	8.93	9.19	8.83	8.67
12a	6903		437	D	222	40	8.22	8.61	8.28	8.28
13	7182	715	278	A	1000	83	9.04	9.19	9.07	9.14
14	7625	443	443	A	1000	83	9.01	9.16	9.01	9.02
14a	7943		318	D	222	40	8.17	8.16	8.19	8.19
15	8173	548	230	A	1000	83	8.97	9.12	9.02	9.04
15a	8459		286	D	222	40	8.36	8.83	8.16	8.16
16	8906	733	447	A	1000	83	9.09	9.24	9.21	9.41
16a	9074		169	D	222	40	7.54	7.84	8.00	8.00
17	9101	195	27	A	1000	55	8.49	8.76	9.01	9.02
17a	9218	117	117	A	1000	55	8.5	8.77	8.99	8.99
18	9795	577	577	A	1000	83	9.08	9.23	9.08	9.15

*From Goldfinger *et al.* (2012).
†Magnitude estimated by this study.

Magnitude–Frequency Distributions for the Cascadia Region

The Cascadia subduction region was not analyzed by Kagan and Jackson (2013) because it was not well defined in the F-E zones. The F-E zone 3 (Figs. 1 and 2) covers California, Nevada, and the southern CSZ but does not include the northern CSZ. Here, we define a new Cascadia region (the rectangular box in Fig. 2) to cover the entire CSZ. The newly defined Cascadia region also covers the Explorer, Juan de Fuca, and Gorda plates; the coordinates of its four corners are (132°, 52°; 123°, 52°; 123°, 39°; 132°, 39°).

As for other subduction zones, we used the Whole Earth model by Kagan and Jackson (2012) to estimate the rate of earthquake occurrence above a lower-threshold magnitude in the zone. We first apply the maximum-likelihood method presented by equation (5) to estimate β-value and corner magnitude for the region. We use the earthquakes in the Global CMT catalog from 1976 to 2012 to compute the log-likelihood function (equation 5). We determine the Global CMT catalog is complete at magnitude 5.5 since 1976 for the region. Figure 3a illustrates the likelihood contour map using $m \geq 5.5$ earthquakes in the Global CMT catalog. The maximum-likelihood β-value is about 0.62 with a very wide 95% confidence range. The maximum-likelihood estimate of the corner magnitude is unreasonably small due to the lack of large earthquakes in the catalog, but the 95% confidence region is essentially

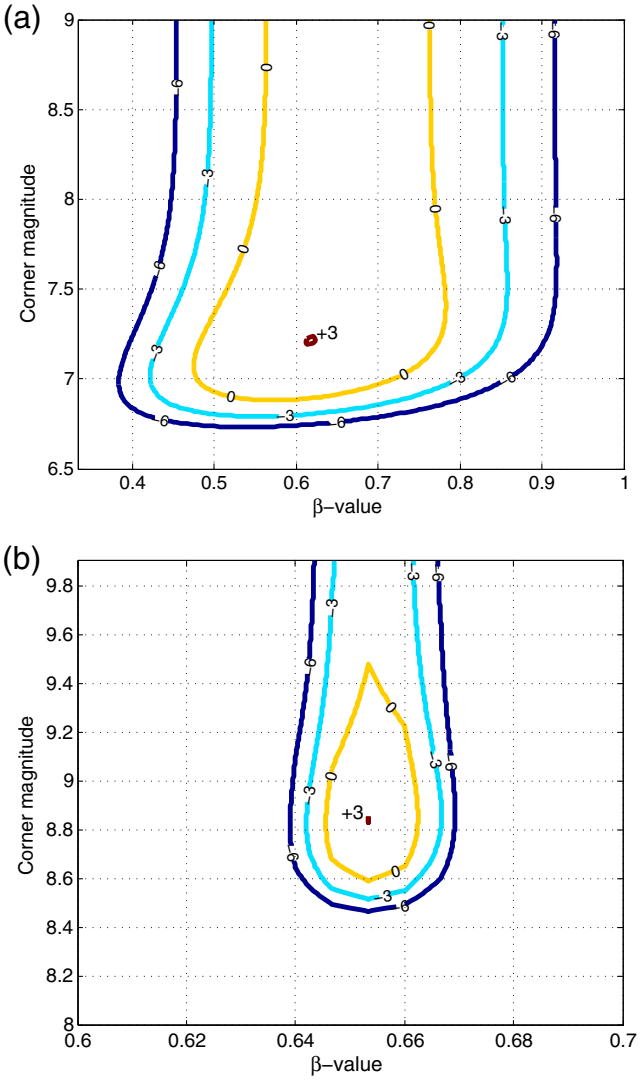

Figure 3. Contour plots of relative log likelihood (l) for tapered Gutenberg–Richter (TGR) distributions for the Cascadia region. For convenience, a constant is added to all values of l to adjust l_{max} to the value of +3, so that the zero contour is approximately the 95% confidence limit. (a) Fit to $m \geq 5.5$ earthquakes in Global Centroid Moment Tensor (CMT) catalog; (b) fit to the combination of Global CMT catalog and turbidite data. The color version of this figure is available only in the electronic edition.

unbounded. That is, the catalog data alone provide no useful upper limit to the corner magnitude.

Because the instrumental catalog is too short to include great CSZ earthquakes, we supplement it with the turbidite-based events (Table 3) to compute the log-likelihood function. We present the results using the magnitudes estimated by Goldfinger *et al.* (2012), because the results from the other alternate sets of magnitudes are similar. To combine the 37-year long (1976–2012) Global CMT catalog with the 10,000-year long turbidite data, we apply a bootstrap technique to the 37-year Global CMT catalog to draw 270 ($10{,}000/37 \approx 270$) bootstrap samples. We assume that the combination of the 270 bootstrap samples represents a 10,000-year medium-to-large event set (with magnitudes smaller than turbidite events). Figure 3b displays the likelihood contour plot using the combined catalog. In this case, both the maximum-likelihood β-value and corner magnitude are well constrained. The maximum-likelihood β-value is about 0.65, same as the generic value for all the subduction zones. The narrow 95% confidence limit of the β-value results from the combination of 270 samples. The maximum-likelihood m_c is 8.84 with a 95% confidence range of 8.6 and 9.5. This exercise demonstrates that combining an instrumental catalog with paleoseismic data is an effective way to solve for magnitude limits for a region.

Because the instrumentally recorded earthquake data are very limited for the CSZ, joint estimation of M_c and β introduces very large uncertainties for both. Thus, we also estimate β separately by a widely used maximum-likelihood technique (Aki, 1965; Bender, 1983; Utsu, 1999; Knopoff, 2000):

$$b = \frac{\log_{10}(e)}{\langle m \rangle - (m_t - \frac{\Delta m_{bin}}{2})} \tag{9}$$

and

$$\sigma_b = \frac{b}{\sqrt{N-1}}, \tag{10}$$

in which Δm_{bin} is the magnitude binning width of the catalog, m_t is the lower threshold magnitude of the catalog, $\langle m \rangle$ is the mean magnitude of the earthquakes equal to or larger than m_t in the catalog, and N is the total number of earthquakes with magnitude equal to or larger than m_t. Using equations (9) and (10), we obtain a β-value of 0.59 ± 0.05. As verification, we estimate the β-value using the m 5.5+ earthquakes after 1990 and obtain the same value but with a slightly larger uncertainty (± 0.06) because the total number of earthquakes is reduced when a shorter time period is used.

The TGR m_c can be estimated using the maximum-likelihood estimate of equation (5) from the combination of instrumental and paleoseismic data, as illustrated in Figure 3b. To be consistent with other zones, we also employed equation (7) to calculate m_c. There are four parameters in the equation:

1. The seismic coupling coefficient, χ. We use 1.0 for this region because geodetic data show that this zone is strongly coupled (Hyndman and Wang, 1995; McCaffrey *et al.*, 2000, 2013; Wang *et al.*, 2003; Scholz and Campos, 2012), and tsunami data require full coupling to fit runup data where present (Witter *et al.*, 2012). Aseismic processes apparently operate only below the coupled zone (Gomberg *et al.*, 2010).
2. The TGR β-value. We use 0.59 as the zone-specific β-value and 0.65 as the generic β-value, like for the other zones.
3. The seismicity rate α_t, which we estimate from the Whole Earth model by Kagan and Jackson (2012).
4. The tectonic moment rate $\dot{M}_T$ of the region, which we estimate using the Global Strain Rate Model v2.0, an update of the model by Kreemer *et al.* (2003).

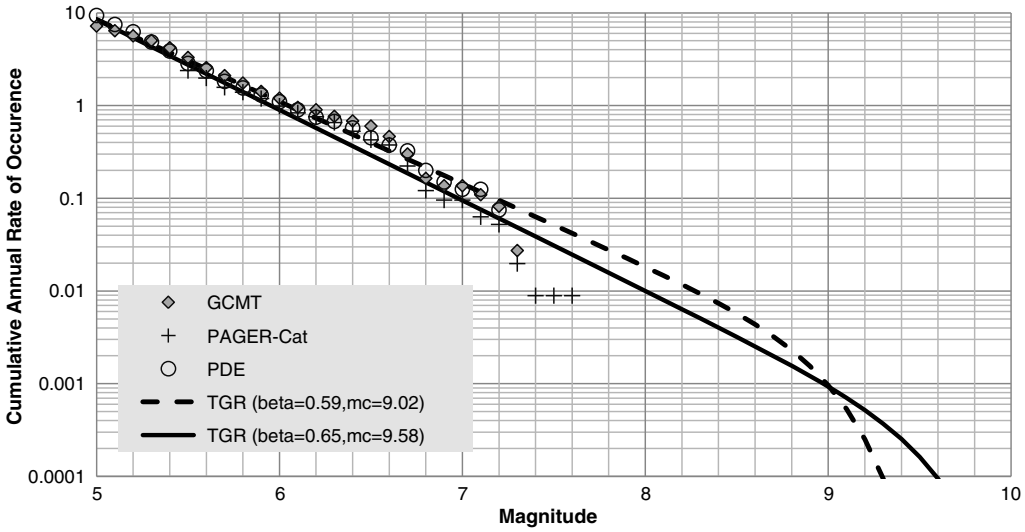

Figure 4. Earthquake magnitude–frequency distributions for the Cascadia region. The dashed curve represents the TGR model with m_c = 9.02 and $\beta = 0.59$. The solid curve represents the TGR model with $m_c = 9.58$ and $\beta = 0.65$.

The seismogenic width in Cascadia is uncertain without a large instrumental event. Thermal, geodetic, structural, and paleoseismic sources of evidence are relatively consistent, suggesting 20 km is a reasonable average value for the variable depth of the down-dip edge of plate coupling. Frankel and Petersen (2013) adopted a similar value for the main branch (weighted 0.5) of the logic tree in the 2014 U.S. national seismic-hazard maps. Lower weightings were assigned to deeper (top of the ETS zone) and shallower alternatives (primarily based on thermal models) based on workshop consensus results. We use an average vertical seismogenic thickness of 20 km and dip of 9° in the tectonic moment rate calculation. We assume the up-dip rupture extends to the seafloor. Thus, the average seismogenic width is about 127 km, consistent with the value calculated using the scaling relationship by Kagan (2002c) for a magnitude 9 earthquake. Some GPS-based models show coupling of the outer accretionary wedge (e.g., McCaffrey *et al.*, 2013), consistent with our assumption. But it is also possible that significant parts of the up-dip accretionary wedge are uncoupled, as discussed in Clarke and Carver (1992), Goldfinger *et al.* (1992, 1997), and Priest *et al.* (2009). For the rigidity, we use 30 GPa. The $\dot{M}_T$ is estimated to be 1.9×10^{20} N·m/year. Using the zone-specific β-value of 0.59, m_c is 9.02. For the generic β-value of 0.65, m_c is 9.58. The m_c values derived from the moment conservation principle are slightly larger than the value derived from purely catalog statistics using the combined instrumental and turbidite earthquakes. The difference can be ascribed to the incompleteness of turbidite events, the magnitude uncertainty of the turbidite events, the uncertainty of the parameters in the tectonic moment rate calculation, and the slight negative bias in our maximum-likelihood method discussed above.

We construct two theoretical TGR magnitude–frequency distributions for the Cascadia region. In the first, we use m_c 9.02 and β-value 0.59 (the dashed curve in Fig. 4), and in the second, we use m_c 9.58 and β-value 0.65 (the solid curve in Fig. 4). We also plot the empirical distributions based on the Global CMT (1976–2012), Prompt Assessment of Global Earthquakes for Response (PAGER-CAT) (1900–2008), and PDE (1973–2012) catalogs. For the PAGER-CAT catalog, the rate of $m \geq 5.5$ is plotted because the catalog does not include many smaller earthquakes. Up to m 7.2, the first model (dashed curve) is fairly consistent with both the Global CMT and PDE catalogs. The PAGER-CAT catalog has a slightly lower rate than the other two catalogs but is more consistent with the second model (solid curve). The largest event in the PAGER-CAT catalog, the 1946 Vancouver Island earthquake, has a magnitude of 7.6 (the 2012 m 7.7 Haida Gwai and the 1949 m 8.1 Queen Charlotte fault earthquakes are outside the rectangular box in Fig. 2). The difference between catalogs is caused by magnitude uncertainties and discrepancies, and the different time periods covered by different catalogs.

The most recent great earthquake in the CSZ is the January 1700 earthquake, estimated to be m 8.7–9.2 (Satake *et al.*, 2003). Turbidite data show an average recurrence of ~500 years for great earthquakes along CSZ (Goldfinger *et al.*, 2012). None of the catalogs includes such large earthquakes given the short times covered by the catalogs. Besides, the region has been very quiet at least since 1900. It is not clear if the post-1900 rate well represents the long-term rate. The turbidite data provide a rare opportunity to verify the tail of the TGR distributions. Hence we plot the distribution of turbidite events together with the TGR distributions in Figure 5. Although the turbidite events with estimated magnitudes < 8.0 may not be complete (Goldfinger *et al.*, 2012), we plot them to demonstrate that events of magnitude 7.5–8.0 did occur along this subduction zone. The 95% confidence limits for the TGR distributions, which are calculated using the Monte Carlo technique discussed below, are also shown. Although there are differences between the four sets of estimated magnitudes, for the magnitude range of $m \geq 8.0$, all the sets fall into the

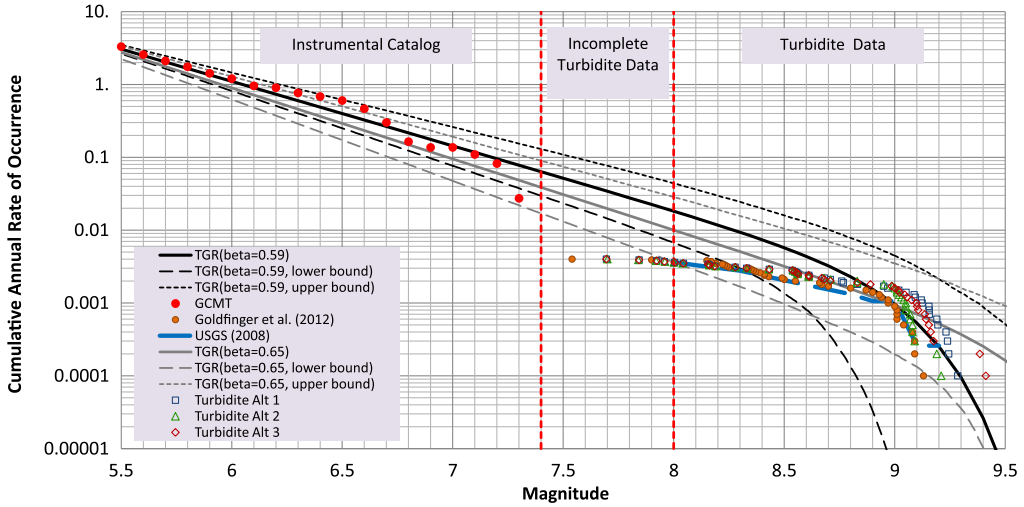

Figure 5. Earthquake magnitude–frequency distributions for the Cascadia region. The solid dots represent the empirical relationship based on the Global CMT catalog. The black curves illustrate TGR distribution with $\beta = 0.59 \pm 0.05$ and $m_c = 9.02 \pm 0.27$ and its 95% confidence limits, and the gray curves illustrate TGR distribution with $\beta = 0.65 \pm 0.05$ and $m_c = 9.58 \pm 0.27$ and its 95% confidence limits. The thick long-dashed curve represents the modeled occurrence of great earthquakes in the 2008 U.S. Geological Survey national seismic-hazard maps (Petersen *et al.*, 2008). The other distributions are based on magnitudes inferred from turbidite data: circles by Goldfinger *et al.* (2012); squares, triangles, and diamonds are based on columns m_{alt1} to m_{alt3} in Table 3. The two vertical dashed lines separate the empirical magnitude–frequency distributions based on the instrumental earthquake data, incomplete turbidite data, and turbidite data, respectively. The color version of this figure is available only in the electronic edition.

95% confidence limit of the TGR with β-value of 0.65. For $m \geq 8.3$, all the sets also fall into the 95% confidence limit of the TGR with β-value of 0.59.

In the USGS 2008 national seismic-hazard maps (Petersen *et al.*, 2008), the primary constraint in the hazard model is that every location in the CSZ is ruptured on average every 500 years, based on the return time of large earthquakes. Two sets of rupture scenarios were considered for the events: (1) m 9.0 $\pm$ 0.2 events that rupture the entire CSZ every 500 years on average and (2) m 8.0–8.7 events with rupture zones that fill the entire zone over a period of about 500 years. A weighing factor of 0.67 was assigned to the m 9.0 $\pm$ 0.2 scenario, and a weighing factor of 0.33 was assigned to the m 8.0–8.7 one. For comparison, we plot the USGS modeled rate in Figure 5. The USGS model lies entirely between the lower bound of 95% confidence limit and median of the TGR with $\beta = 0.65$. For the magnitude range of 8.4–9.2, the USGS model falls between the lower bound of 95% confidence limit and median TGR models of $\beta = 0.59$.

Nevertheless, the discrepancy between the paleoseismic data and the theoretical TGR models cannot be ignored: the median TGR models predict more $m < 8.5$ earthquakes than observed by turbidite data. There are several possible reasons for the discrepancy:

1. The turbidite record may not be complete at magnitudes less than 8.5. Goldfinger *et al.* (2012) believed that the turbidite record is complete at $m \sim 8$. They reported about 20 earthquakes that ruptured only the southern and/or southern and central CSZs, but they did not find any evidence of events that ruptured only the northern CSZ. On the other hand, Atwater and Griggs (2012) discuss additional tsunami evidence from Discovery Bay, along the eastern Juan de Fuca strait in northern Washington, for an event that does not correspond in time with Pacific coastal evidence of whole-CSZ rupture events. A greater frequency of far northern plate boundary earthquakes would help explain the roughly 300-year average interval between inferred tsunamis at Discovery Bay (Atwater and Griggs, 2012). However, Goldfinger, Beeson, *et al.* (2013) searched archive cores for such evidence and found only a small number of potential northern events; these had been previously reported by Adams (1990). Atwater and Griggs (2012) argued that gentle slopes and a broad continental shelf may put northern Cascadia cores at a disadvantage in recording small turbidite deposits. However, a new analysis of continental slope cores in Washington shows that the upper slope cores, in areas with steeper slopes and higher sediment supply, contain only a few potential northern events not previously reported (Goldfinger, Beeson, *et al.*, 2013; Goldfinger, Morey, *et al.*, 2013). Furthermore, Enkin *et al.* (2013) show that in a highly sensitive fiord site with very steep sidewalls, no extra turbidites are observed beyond those correlated to the offshore record, other than the 1946 Vancouver Island earthquake. Nevertheless, if more events of m 7–8 are eventually confirmed, the $m < 8.5$ gap between turbidite data and TGR curves in Figure 5 could be reduced.
2. Some turbidite flows believed caused by magnitude 9 events might have been caused by multiple smaller events

Table 4
Results of $m_p(T)$ from Different TGR Models for the CSZ

TGR Models	In 50 years		In 100 years		In 250 years		In 500 years		In 1000 years		In 10,000 years	
	m_p	σ	m_p	σ	m_p	σ	m_p	σ	m_p	σ	m_p	σ
$\beta = 0.59$ $m_c = 9.02$	7.94	0.20	8.25	0.21	8.59	0.20	8.80	0.20	8.96	0.21	9.29	0.23
$\beta = 0.65$ $m_c = 9.58$	7.69	0.18	8.00	0.20	8.40	0.22	8.69	0.22	8.95	0.22	9.56	0.22

closely spaced in time. In fact, event T5 is such a candidate (Goldfinger *et al.*, 2012).

3. The TGR curves represent the occurrence of all the shallow earthquakes in the rectangular box in Figure 2, including events related to structures other than the CSZ. There is potential of m 8 earthquakes along the Mendocino and Blanco fracture zones and the fault structures to the north. However, the turbidite-based events were likely only related to the subduction zone.
4. The large earthquakes in the CSZ might not follow the TGR distribution. However, they do not follow obviously slip or time-predictable models, either (Goldfinger, Ikeda, *et al.*, 2013). Earthquake clusters and gaps are observed during the 10,000-year event history (Goldfinger *et al.*, 2012). Goldfinger, Ikeda, *et al.* (2013) suggested that those features represent long-term supercycles in the subduction zone.
5. There could be substantial temporal variation in the earthquake rate at all magnitudes. Goldfinger, Ikeda, *et al.* (2013) observe temporal variations in large magnitude events, but similar variations may exist for other magnitudes that have not been observed in the seismic recordings of the last century.
6. It is very difficult to infer magnitudes of paleoearthquakes from the turbidite data. Because many assumptions were involved, the inferred magnitudes are subject to large uncertainties.

Whatever the cause of the apparent discrepancies, there is no question that the turbidite data and onshore paleoseismic evidence imply that huge earthquakes, magnitude 9 or greater, have occurred along the CSZ. Any magnitude–frequency model must accept large uncertainties because of the limited data and reliance on proxy information, but such models are required to estimate probable magnitudes over different time periods.

We summarize the results of CSZ $m_p(T)$ derived from different TGR models in Table 4. The two TGR models intersect at $m_p(1000)$ but diverge at both shorter and longer return periods. The result of $m_p(500) = 8.7$ or 8.8 does not conflict with the general statement that "the return time of $m \sim 9$ earthquakes is ~500 years" because the former comes from a TGR distribution and the latter implies a characteristic model. In fact, the median TGR models predict the same rate as the USGS model at m 9.0 and a higher rate at magnitudes lower and higher than 9.0 (Fig. 5).

Results

Uncertainty Estimation

We construct TGR distributions for the circum-Pacific F-E subduction zones. For each region, we calculate the rate of events larger than the threshold magnitude ($m_t = 5.0$) by summing up the smoothed rate density in the Whole Earth model on each $0.1° \times 0.1°$ grid multiplied by the area of the grid. For all the regions but the CSZ, the β-value and the corner magnitude listed in Table 2 were used to construct the TGR distributions. Because the largest earthquakes are usually subduction interplate earthquakes, only shallow earthquakes (depth less than 70 km) in the catalogs are considered in this study.

Because m_p is determined by a TGR curve, it is a function of three input variables: r_t (the rate of earthquakes larger than a threshold magnitude), the TGR β-value, and m_c. We propagate the uncertainties in the three input variables into the uncertainty of m_p. Among the three input variables, r_t and β are positively correlated. We performed a sensitivity test on the correlation of the two parameters. Our results show that, from noncorrelated (correlation coefficient is 0) to fully correlated (correlation coefficient is 1), the change of m_p is less than 0.03 magnitude units. The change of $\sigma(m_p)$ is less than 0.1 for all the zones except the CSZ, in which $\sigma(m_p)$ reduces from 0.28 to 0.14 when correlation is changed from weak to strong. Thus, we adopt a correlation coefficient of 0.5 for our calculations.

We use Monte Carlo simulation to calculate the uncertainty of m_p for each of the F-E zones. We assume normal distributions for β and m_c. The mean and uncertainty of β and m_c are from Table 2. The mean value of r_t is calculated from the Whole Earth model (Kagan and Jackson, 2012). The standard deviation of r_t is estimated by $\sqrt{r_t T_{cat}}/T_{cat}$, in which T_{cat} is the historical earthquake catalog duration used in the Whole Earth model. The underlying assumption of this standard deviation is that the occurrence of $m \geq 5.0$ earthquakes during the catalog time follows the Poisson distribution. We simulate 2000 r_t, β, and m_c sets for each of the subduction zones. For each of the 2000 simulations, a TGR distribution is created, and m_p for each return period of interest is calculated so that we obtain a distribution of m_p at each of the return periods (e.g., Fig. 6).

Maximum Probable Earthquake Magnitude Using Zone-Specific β-values

Table 5 summarizes the estimated median of m_p and uncertainties for return periods of 50, 100, 250, and 500 years

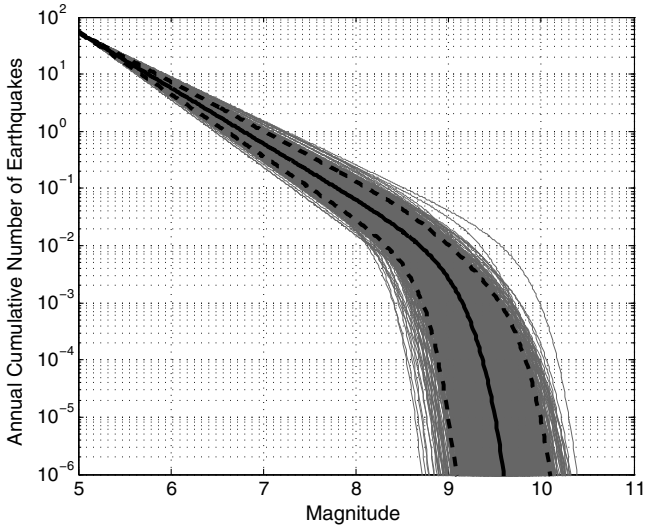

Figure 6. TGR distributions for the Alaska–Aleutian subduction zone (F-E zone 1). Each of the thin gray curves represents one of the 2000 simulations. The solid black curve is created using the mean values of β, m_c, and r_t. The two dashed black curves represent the 95% confidence limits of the TGR distribution based on the 2000 simulations.

estimated using zone-specific β and the corresponding m_c values. Except for Guam–Japan (F-E zone 18), the estimated m_p exceeds 7.9 at 50-year, 8.2 at 100-year, 8.5 at 250-year, and 8.6 at 500-year return periods. The 50-year m_p is equal to or larger than 8.4 for the Alaska–Aleutian arc, Andean South America, New Hebrides Islands, Bismarck–Solomon Islands, New Guinea, Japan–Kamchatka, and Sunda arc regions. For the Andean South America and Japan–Kamchatka regions, the 100-year m_p is about 8.9. The 250-year m_p is greater than 9.0 for Andean South America, New Guinea, Japan–Kamchatka, and Sunda arc. The 500-year m_p is about 9.0 or larger for the Alaska–Aleutian arc, Andean South America, New Guinea, Japan–Kamchatka, southeast Japan–Ryukyu Islands, Borneo–Celebes, and Sunda arc. Most of the uncertainties of m_p are 0.2–0.3 magnitude units, which is about the uncertainty of m_c. However, the uncertainty is larger for the Caribbean Loop, Guam–Japan, and southeast Japan–Ryukyu Islands due to relatively high uncertainties on the β-values and m_c and relatively low seismic activity.

We compare the estimated m_p with the available historical maximum magnitudes m_h (Table 5 and Fig. 7). The m_h is collected from three sources: the PAGER-CAT catalog (Allen *et al.*, 2009), the Centennial catalog (Engdahl and Villaseñor, 2002), and the Global Large Historical Earthquake catalog (GLHECAT; Albini *et al.*, 2014) by the Global Earthquake Model (GEM) project. For each event listed in the PAGER-CAT and Centennial catalogs, multiple magnitudes are reported, and a preferred magnitude is selected by the catalog authors. In the table and figure, we use the preferred magnitude from the PAGER-CAT catalog and the largest reported magnitude from the Centennial catalog. We take the former as a proxy of the median m_h and the latter as a proxy of the upper bound of m_h. The GLHECAT includes global large ($m \geq 7.0$) earthquakes from A.D. 1000 to A.D. 1903. If the maximum magnitude in the pre-1900 catalog is larger than the historical m_h from the PAGER-CAT and Centennial catalogs, the pre-1900 magnitude is listed in the table and shown in the figure.

Using the preferred magnitude in the PAGER-CAT catalog, 6 of the m_h after 1900 are larger than the $m_p(100)$, whereas 12 are smaller. Using the largest magnitude in the Centennial catalog, the m_h since 1900 in 11 zones falls between the 50-year and 250-year expected m_p. Is the observed m_h consistent with the estimated m_p? To answer this question, we apply the two-tail paired Student's t-test to the $m_p(100)$ and m_h since 1900. Using the PAGER-CAT m_h, a p-value of 0.23 is obtained. Using the Centennial m_h, a p-value of 0.36 is obtained. This means that we cannot reject the hypothesis at the 95% confidence level that the observed m_h is consistent with the estimated m_p for either catalog.

Maximum Probable Earthquake Magnitude Based on the Generic β-Value

We adopted the generic β-value of 0.65 for all the zones and the corresponding m_c to estimate m_p. The results are shown in Table 6. We again applied the two-tail paired Student's t-test to the $m_p(100)$ based on the generic β-value and m_h since 1900. Using the PAGER-CAT's m_h, a p-value of 0.06 was obtained. Using the Centennial's m_h, a p-value of 0.80 was obtained. Therefore, we cannot reject the hypothesis at 95% confidence level that the observed m_h is consistent with the m_p estimated from the generic β-value.

Discussion

The b-value (or β-value) is an important parameter in seismic-hazard analysis because small changes in b-value can result in large changes in the projected numbers of major earthquakes. The debate of universal or nonuniversal b-values across different regions has been going on for years. Schorlemmer *et al.* (2005) showed the b-value varies systematically for different styles of faulting. Kagan (1999) and Kagan and Jackson (2013) state that statistically β-values are approximately the same for all regions. Figure 8 compares the m_p estimated from zone-specific and generic β-values at 50-, 100-, 250-, 500-, 1000-, and 10,000-year return periods. The differences are small for most of the regions but significant for a few regions. For example, in Andean South America, where the 1960 m 9.6 Chile earthquake occurred, the $m_p(10{,}000)$ is about 9.7 using the generic β-value and only about 9.3 if the zone-specific β-value is used. The Guam–Japan region is another example of a large difference: the m_p based on the generic β-value is 0.7–0.9 magnitude units larger than that based on the zone-specific β-value for 50- to 1000-year return periods.

The faulted Earth working group of the GEM project characterized geometry, coupling coefficients, upper and lower depth, plate motions, maximum earthquake magnitudes,

Table 5
Estimated m_p Using Specific β-Values for the Circum-Pacific Subduction Zones

	In 50 years		In 100 years		In 250 years		In 500 years		PAGER-CAT		Centennial Cat.		GLHECAT		
F-E ID	m_p	σ	m_p	σ	m_p	σ	m_p	σ	Year	m_h	Year	m_h	Year	m_h	Name
1	8.43	0.17	8.66	0.17	8.90	0.18	9.04	0.19	1964	9.2	1964	9.2			Alaska–Aleutian arc
3*	7.94	0.20	8.25	0.21	8.59	0.20	8.80	0.20	1946	7.6	1946	7.6	1700	9.0	Cascadia
5	8.19	0.22	8.38	0.21	8.56	0.22	8.67	0.22	1985	8.0	1902	8.4	1787	8.4	Mexico–Guatemala
6	7.93	0.21	8.21	0.22	8.54	0.22	8.75	0.21	1950	7.8	1904	8.3			Central America
7	7.95	0.35	8.22	0.34	8.51	0.31	8.67	0.29	1946	7.9	1900	8.4	1842	8.2	Caribbean Loop
8	8.74	0.19	8.89	0.20	9.03	0.22	9.12	0.23	1960	9.6	1960	9.6			Andean South America
12	8.08	0.14	8.33	0.15	8.66	0.17	8.90	0.18	1917	8.5	1917	8.7			Kermadec–Tonga–Samoa
14	8.39	0.20	8.49	0.22	8.59	0.23	8.65	0.24	1901	7.9	1901	8.4			New Hebrides Islands
15	8.39	0.19	8.49	0.21	8.59	0.23	8.65	0.23	1971	8.1	1906	8.4			Bismarck–Solomon Islands
16	8.47	0.23	8.75	0.24	9.08	0.23	9.28	0.22	1996	8.2	1906	8.4			New Guinea
18	7.34	0.27	7.57	0.30	7.88	0.33	8.11	0.36	1914	7.9	1902	8.1	1498	8.3	Guam–Japan
19	8.72	0.18	8.87	0.19	9.01	0.21	9.10	0.22	2011	9.0	1952	9.0			Japan–Kamchatka
20	8.11	0.44	8.41	0.43	8.75	0.40	8.95	0.37	1911	8.1	1946	8.4	1707	8.6	S.E. Japan–Ryukyu Islandsa
21	8.03	0.25	8.27	0.24	8.53	0.23	8.68	0.23	1920	7.9	1920	8.0			Taiwan
22	8.26	0.19	8.5	0.19	8.76	0.19	8.92	0.20	1918	8.2	1918	8.3			Philippines
23	8.31	0.20	8.55	0.20	8.82	0.20	8.99	0.20	1965	8.2	1939	8.6			Borneo–Celebes
24	8.53	0.17	8.77	0.17	9.03	0.18	9.18	0.19	2007	8.5	1938	8.6	1833	8.7	Sunda arc
46	8.03	0.28	8.30	0.29	8.66	0.30	8.90	0.29	2004	9.0	2004	9.0			Andaman Island Sumatra

*Results are for the redefined Cascadia region (Fig. 2).

and other parameters for all 55,000 km of the subduction zones in the world (Berryman *et al.*, 2013). They divided the subduction zones into 65 individual segments and estimated minimum and maximum m_x for each segment, based on the largest observed magnitudes and tectonic moment rate, respectively. They then assigned a preferred m_x, which is the average of the minimum and maximum m_x. We map their segments into the F-E zones and read the preferred and maximum m_x values among the segments within one F-E zone. McCaffrey (2008) also estimated the maximum earthquake magnitudes and their recurrence time for all of the subduction zones in the world. We relate the values in McCaffrey (2008) to the F-E zones. We compare the GEM preferred and maximum m_x, McCaffrey's m_x, and $m_p(1000)$ and $m_p(10{,}000)$ from this study (Fig. 9). The comparison reveals that:

- Most of the GEM preferred m_x are lower than the $m_p(1000)$ from this study, but most of the GEM maximum m_x are between $m_p(1000)$ and $m_p(10{,}000)$.
- The m_x values by McCaffrey (2008) are much higher than our $m_p(1000)$ values but fairly consistent with $m_p(10{,}000)$. However, most of the recurrence times of the great earthquakes by McCaffrey (2008) are in the range of hundreds to thousands of years. This implies that McCaffrey (2008)

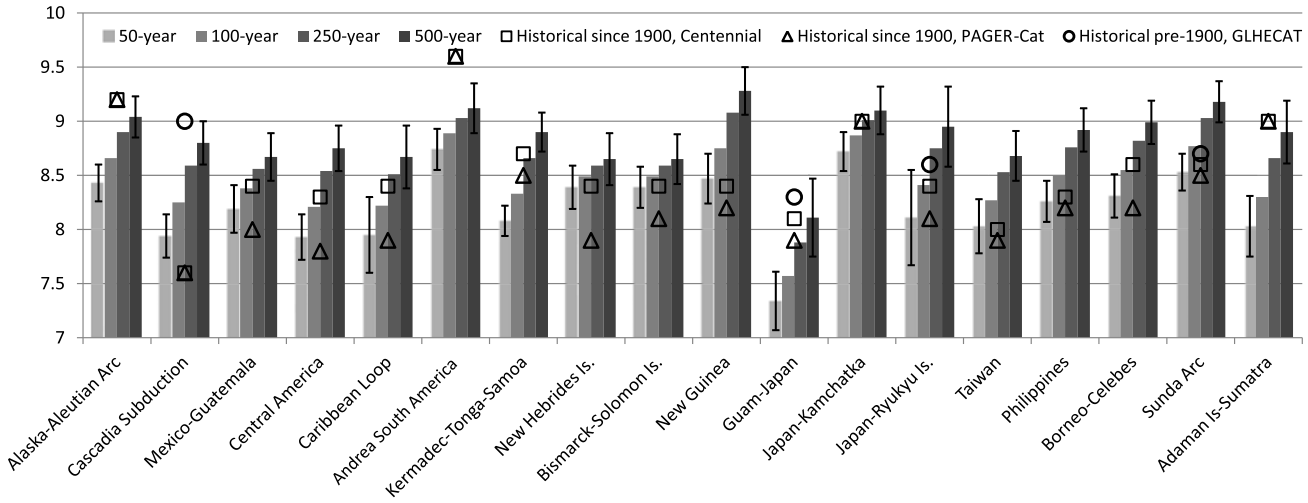

Figure 7. The estimated m_p for 50-, 100-, 250- and 500-year return periods for the subduction zones. Zone-specific β-values are used for estimating $m_p(T)$ values. Uncertainties ($\pm 1\sigma$; black bars) are shown only for 50- and 500-year return periods. The historical maximum magnitudes are from the Centennial, PAGER-CAT, and GLHECAT catalogs.

Table 6
Estimated m_p for 50-, 100-, 250-, and 500-year Return Periods for the Circum-Pacific Subduction Zones Using the Generic β-value

	In 50 years		In 100 years		In 250 years		In 500 years		PAGER-CAT		Centennial Cat.		GLHECAT		
F-E ID	m_p	σ	m_p	σ	m_p	σ	m_p	σ	Year	m_h	Year	m_h	Year	m_h	Name
1	8.43	0.17	8.66	0.17	8.90	0.18	9.04	0.19	1964	9.2	1964	9.2			Alaska–Aleutian arc
3*	7.69	0.18	8.00	0.20	8.40	0.22	8.69	0.22	1946	7.6	1946	7.6	1700	9.0	Cascadia
5	8.07	0.23	8.31	0.23	8.58	0.22	8.74	0.22	1985	8.0	1902	8.4	1787	8.4	Mexico–Guatemala
6	8.05	0.22	8.31	0.21	8.59	0.21	8.76	0.21	1950	7.8	1904	8.3			Central America
7	7.84	0.35	8.12	0.36	8.46	0.34	8.67	0.32	1946	7.9	1900	8.4	1842	8.2	Caribbean Loop
8	8.57	0.19	8.83	0.19	9.11	0.19	9.28	0.19	1960	9.6	1960	9.6			Andean South America
12	8.54	0.17	8.69	0.18	8.85	0.20	8.94	0.22	1917	8.5	1917	8.7			Kermadec–Tonga–Samoa
14	8.41	0.16	8.57	0.18	8.72	0.20	8.81	0.22	1901	7.9	1901	8.4			New Hebrides Islands
15	8.42	0.16	8.57	0.18	8.71	0.20	8.79	0.22	1971	8.1	1906	8.4			Bismarck–Solomon Islands
16	8.52	0.24	8.79	0.24	9.09	0.23	9.28	0.22	1996	8.2	1906	8.4			New Guinea
18	8.09	0.44	8.39	0.44	8.76	0.42	9.00	0.40	1914	7.9	1902	8.1	1498	8.3	Guam–Japan
19	8.70	0.17	8.88	0.18	9.07	0.19	9.18	0.21	2011	9.0	1952	9.0			Japan–Kamchatka
20	7.98	0.44	8.28	0.45	8.66	0.44	8.91	0.42	1911	8.1	1946	8.4	1707	8.6	S.E. Japan–Ryukyu Islands
21	7.99	0.25	8.25	0.24	8.52	0.23	8.68	0.23	1920	7.9	1920	8.0			Taiwan
22	8.34	0.19	8.54	0.19	8.75	0.20	8.87	0.21	1918	8.2	1918	8.3			Philippines
23	8.39	0.20	8.60	0.20	8.82	0.20	8.94	0.21	1965	8.2	1939	8.6			Borneo–Celebes
24	8.53	0.17	8.77	0.17	9.03	0.18	9.18	0.19	2007	8.5	1938	8.6	1833	8.7	Sunda arc
46	8.27	0.28	8.52	0.27	8.78	0.25	8.93	0.23	2004	9.0	2004	9.0			Andaman Island –Sumatra

*Results are for the redefined Cascadia region (Fig. 2).

estimated much higher rates for such earthquakes than this study.

- The GEM preferred m_x is extremely low for the Central America and Guam–Japan regions. Both subduction zones are characterized by rapid plate convergence and high rates of seismicity but have been associated with few great ($m > 8.0$) interplate earthquakes. Pacheco *et al.* (1993) obtained low seismic coupling for both subduction zones based on the observed seismicity. The weak coupling along the Central America subduction zone is also supported by GPS studies (Correa-Mora *et al.*, 2009). Nevertheless, the estimation of coupling is far from reliable, especially based on the short history of earthquakes, and even very low rates of strain accumulation may result in a large earthquake, given enough time (Goldfinger, Ikeda, *et al.*, 2013).

Although the statistical tests cannot reject the hypothesis that the estimated m_p is consistent with the historical observations, the historical earthquake catalog is not long enough to verify the m_p. However, paleoseismic data can extend the earthquake record back thousands of years. The turbidite sediments extracted from the deep sea channels of the CSZ preserve about a 10,000-year earthquake history for that subduction zone, which can be used to verify and constrain the recurrence rate of great earthquakes. It would be useful to collect paleoseismic data for all of the major subduction zones to obtain return times.

Conclusions

Because the traditional methods for estimating m_x are inadequate and m_x itself is ill-defined, we use $m_p(T)$, probable maximum magnitude within a time period of T, to replace m_x We develop a method to estimate $m_p(T)$ for each of the circum-Pacific subduction zones. In our method, we fit a TGR distribution to historical catalogs for each of the zones. The two parameters of the TGR distribution are determined by maximum-likelihood method and moment conservation principle. The rate of earthquakes for each zone, which is also required to estimate $m_p(T)$, is calculated using the Whole Earth model (Kagan and Jackson, 2012). We use Monte-Carlo simulation to estimate uncertainties in the TGR parameters.

Our results show that most of the circum-Pacific subduction zones can generate $m \geq 8.5$ earthquakes over a 250-year return period. Over a 500-year return period, most of the zones can generate $m \geq 8.8$ earthquakes. Over a 10,000-year return period, almost all of the zones can generate $m \geq 9.0$ earthquakes. The β-value (or b-value) is an important parameter in statistical seismology and seismic-hazard analysis. The debate of universal or locally varying β-values (or b-values) is still ongoing. In general, the $m_p(T)$ determined using universal and local β-values are similar.

We compare our results with the largest historical earthquake magnitudes in each of the subduction zones. We conclude that the hypothesis that the estimated $m_p(100)$ is consistent with the observations since 1900 cannot be rejected by statistical tests. Unfortunately, the historical earthquake catalogs are too short to verify our results for longer T.

Submarine turbidite records unearth a ~10,000-year paleoseismic history of great earthquakes along the CSZ. We collate the paleoseismic data and estimate the magnitudes. We compare the magnitude–frequency distribution of the great earthquakes with our TGR models. At 95% confidence level, our models and the data are consistent, which gives us confidence about our methodology.

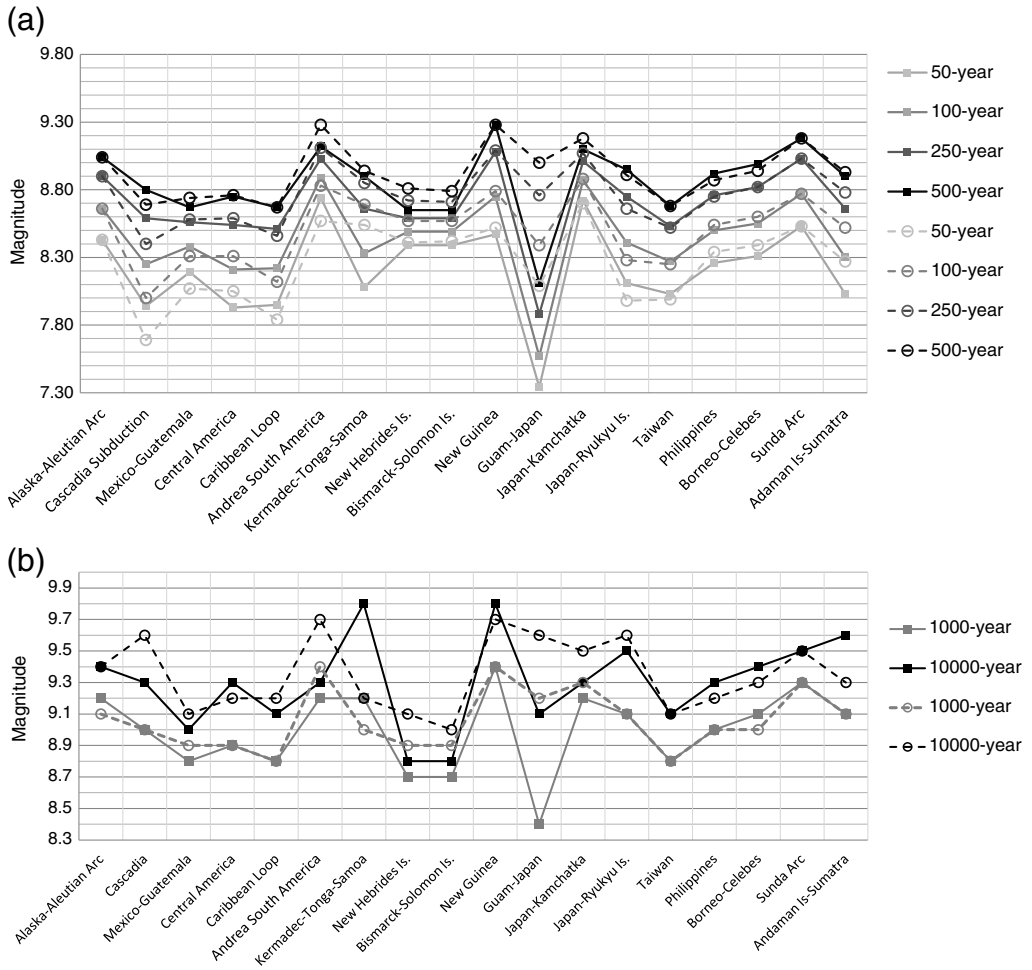

Figure 8. The estimated m_p for different return periods for the subduction zones. The squares (connected by solid lines) are based on zone-specific m_c and β-values, and the circles (connected by dashed lines) are based on generic β-values and the corresponding m_c: (a) For 50-, 100-, 250-, and 500-year return periods; and (b) for 1000- and 10,000-year return periods.

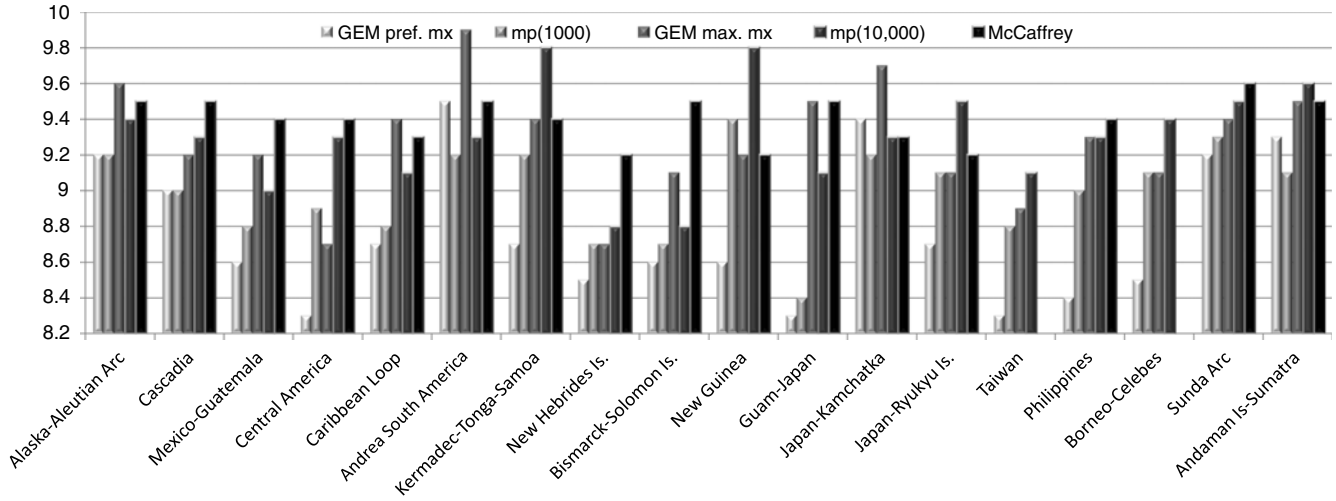

Figure 9. Comparisons of $m_p(T)$ from this study to the m_x by McCaffrey (2008) and GEM (Berryman *et al.*, 2013). The $m_p(T)$ values are based on the zone-specific β-values.

McCaffrey (2008) examined worldwide subduction zones and stated that current evidence cannot rule out that any subduction zone may produce a magnitude 9 or larger earthquake. Our study demonstrates that $m \sim 9$ earthquakes are expected along any of the circum-Pacific subduction zones given a sufficient period of time (~10,000 years).

Data and Resources

The Global Centroid Moment Tensor catalog (Dziewonski *et al.*, 1981; Ekström *et al.*, 2005, 2012) is available at http://www.globalcmt.org/CMTfiles.html. The Centennial catalog (Engdahl and Villaseñor, 2002) is available at http://earthquake.usgs.gov/data/centennial/. The PAGER-CAT earthquake catalog (Allen *et al.*, 2009) is available at http://earthquake.usgs.gov/research/pager/data/. The PDE catalog (National Earthquake Information Center [NEIC], 1970; Sipkin *et al.*, 2000) is available at ftp://hazards.cr.usgs.gov/pde/ or as an online search at http://neic.usgs.gov/neis/epic/epic_global.html. Flinn–Engdahl regions are explained and their coordinates as well as FORTRAN files to process them are available at http://earthquake.usgs.gov/learn/topics/flinn_engdahl_list.php. All the electronic addresses referenced here were last accessed August 2014.

Acknowledgments

The authors are grateful for the constructive comments from FM Global colleagues: Hosam Ali, Franco Tamanini, and Lou Gritzo. We thank Yan Kagan and Peter Bird from the University of California, Los Angeles (UCLA), and Ross Stein from U.S. Geological Survey (USGS) for useful discussions. We also thank Kelvin Berryman from GNS Science of New Zealand, Marco Pagani from Global Earthquake Model (GEM), and Paola Albini from Istituto Nazionale di Geofisica e Vulcanologia (INGV) of Italy for generously sharing data and results. We appreciate the USGS John Wesley Powell Center for Analysis and Synthesis for providing us opportunities to discuss the project at meetings supported by the Center. We are grateful to Associate Editor Matt Gerstenberger and two anonymous reviewers for their reviews and comments, which significantly improved the manuscript. This work was funded by FM Global.

References

Adams, J. (1990). Paleoseismicity of the Cascadia subduction zone: Evidence from turbidites off the Oregon-Washington margin, *Tectonics* **9,** 569–583, doi: 10.1029/TC009i004p00569.

Aki, K. (1965). Maximum likelihood estimate of b in the formula $\log(N) = a–bM$ and its confidence limits, *Bull. Earthq. Res. Inst. Tokyo Univ.* **43,** 237–239.

Albini, P., R. M. W. Musson, A. Rovida, M. Locati, A. A. Gomez Capera, and D. Viganò (2014). The global earthquake history, *Earthq. Spectra* **30,** 607–624.

Allen, T. I., K. Marano, P. S. Earle, and D. J. Wald (2009). PAGER-CAT: A composite earthquake catalog for calibrating global fatality models, *Seismol. Res. Lett.* **80,** no. 1, 50–56.

Atwater, B. F. (1987). Evidence for great Holocene earthquakes along the outer coast of Washington State, *Science* **236,** 942–944.

Atwater, B. F., and G. B. Griggs (2012). Deep-sea turbidites as guides to Holocene earthquake history at the Cascadia Subduction Zone—Alternative views for a seismic-hazard workshop, *U.S. Geol. Surv. Open-File Rept. 2012-1043*, 58 pp., available at http://pubs.usgs.gov/of/2012/1043/ (last accessed October 2013).

Atwater, B. F., A. R. Nelson, J. J. Clague, G. A. Carver, D. K. Yamaguchi, P. T. Bobrowsky, J. Bourgeois, M. E. Darienzo, W. C. Grant, and E. Hemphill-Haley et al. (1995). Summary of coastal geologic evidence for past great earthquakes at the Cascadia subduction zone, *Earthq. Spectra* **11,** 1–18.

Bell, A. F., M. Naylor, and I. G. Main (2013). Convergence of the frequency-size distribution of global earthquakes, *Geophys. Res. Lett.* **40,** 2585–2589, doi: 10.1002/grl.50416.

Bender, B. (1983). Maximum likelihood estimation of b values for magnitude grouped data, *Bull. Seismol. Soc. Am.* **73,** 831–851.

Berryman, K., L. Wallace, G. Hayes, P. Bird, K. Wang, R. Basili, T. Lay, R. Stein, T. Sagiya, C. Rubin, S. Barreintos, C. Kreemer, N. Litchfield, M. Pagani, K. Gledhill, K. Haller, and C. Costa (2013). *The GEM Faulted Earth Subduction Characterisation Project, Version 1.0*, June 2013, GEM Faulted Earth Project, available at http://www.nexus.globalquakemodel.org/gem-faulted-earth/posts (last accessed October 2013).

Bird, P., and Y. Y. Kagan (2004). Plate-tectonic analysis of shallow seismicity: Apparent boundary width, beta, corner magnitude, coupled lithosphere thickness, and coupling in seven tectonic settings, *Bull. Seismol. Soc. Am.* **94,** no. 6, 2380–2399.

Bird, P., and Z. Liu (2007). Seismic hazard inferred from tectonics: California, *Seismol. Res. Lett.* **78,** no. 1, 37–48.

Bird, P., C. Kreemer, and W. E. Holt (2010). A long-term forecast of shallow seismicity based on the Global Strain Rate Map, *Seismol. Res. Lett.* **81,** no. 2, 184–194, doi: 10.1785/gssrl.81.2.184.

Chapman, J. S., and T. I. Melbourne (2009). Future Cascadia megathrust rupture delineated by episodic tremor and slip, *Geophys. Res. Lett.* **36,** doi: 10.1029/2009GL040465.

Clarke, S. H., and G. A. Carver (1992). Breadth of interplate coupling in the southern Cascadia subduction zone: Implication for earthquake magnitudes, *Geol. Soc. Am. Abs. Prog.* **24,** 15.

Correa-Mora, F., C. DeMets, D. Alvarado, H. L. Turner, G. Mattioli, D. Hernandez, C. Pullinger, M. Rodriguez, and C. Tenorio (2009). GPS-derived coupling estimates for the Central America subduction zone and volcanic arc faults: El Salvador, Honduras and Nicaragua, *Geophys. J. Int.* **179,** 1279–1291. doi: 10.1111/j.1365-246X.2009.04371.x.

Dziewonski, A. M., T. A. Chou, and J. H. Woodhouse (1981). Determination of earthquake source parameters from waveform data for studies of global and regional seismicity, *J. Geophys. Res.* **86,** 2825–2852.

Earthquake Research Committee (2005). *National Seismic Hazard Maps for Japan*, available at http://www.jishin.go.jp/main/index-e.html (last accessed October 2013).

Ekström, G., A. M. Dziewonski, N. N. Maternovskaya, and M. Nettles (2005). Global seismicity of 2003: Centroid-moment-tensor solutions for 1087 earthquakes, *Phys. Earth Planet. Int.* **148,** 327–351.

Ekström, G., M. Nettles, and A. M. Dziewonski (2012). The global CMT project 2004–2010: Centroid-moment tensors for 13017 earthquakes, *Phys. Earth Planet. Int.* **200/201,** 1–9.

Engdahl, E. R., and A. Villaseñor (2002). Global seismicity: 1900–1999, in *International Handbook of Earthquake Engineering and Seismology*, W. K. Lee, H. Kanamori, P. C. Jennings, and C. Kisslinger (Editors), Academic Press, Amsterdam, Netherlands, 665–690.

Enkin, R. J., A. Dallimore, J. Baker, J. R. Southon, and T. Ivanochko (2013). A new high-resolution radiocarbon Bayesian age model of the Holocene and Late Pleistocene from core MD02-2494 and others, Effingham Inlet, British Columbia, Canada; with an application to the paleoseismic event chronology of the Cascadia Subduction Zone, *Can. J. Earth Sci.* **50,** 746–760.

Flinn, E. A., and E. R. Engdahl (1965). A proposed basis for geographical and seismic regionalization, *Rev. Geophys.* **3,** 123–149.

Flinn, E. A., E. R. Engdahl, and A. R. Hill (1974). Seismic and geographical regionalization, *Bull. Seismol. Soc. Am.* **64,** 771–993.

Flück, P., R. D. Hyndman, and K. Wang (1997). 3-D dislocation model for great earthquakes of the Cascadia subduction zone, *J. Geophys. Res.* **102,** 20,539–20,550.

Frankel, A., C. Mueller, T. Barnhard, D. Perkins, E. Leyendecker, N. Dickman, S. Hanson, and M. Hopper (1996). National Seismic Hazard Maps—Documentation, *U.S. Geol. Surv. Open-File Rept. 96-532*, 110 pp.

Frankel, A. D., and M. D. Petersen (2013). *Appendix P: Models of Earthquake Recurrence and Down-Dip Edge of Rupture for the Cascadia Subduction Zone*, http://pubs.usgs.gov/of/2013/1165/ (last accessed August 2014).

Frankel, A. D., M. D. Petersen, C. S. Mueller, K. M. Haller, R. L. Wheeler, E. V. Leyendecker, R. L. Wesson, S. C. Harmsen, C. H. Cramer, D. M. Perkins, and K. S. Rukstales (2002). Documentation for the 2002 update of the National Seismic Hazard Maps, *U.S. Geol. Surv. Open-File Rept. 2002-420*, 39 pp.

Furlong, K. P., T. Lay, and C. J. Ammon (2009). A great earthquake rupture across a rapidly evolving three-plate boundary, *Science* **324,** 226–229, doi: 10.1126/science.1167476.

Gaull, B. A., M. O. Michael-Leiba, and J. M. W. Rynn (1990). Probabilistic earthquake risk maps of Australia, *Aust. J. Earth Sci.* **37,** 169–187.

Goldfinger, C., J. Beeson, H. Nelson, J. R. Patton, A. Morey, and S. Galer (2013). Cascadia seismoturbidities: A landlubber critiqued (Abstract), *2013 Fall Meeting, AGU*, San Francisco, California, 9–13 December.

Goldfinger, C., Y. Ikeda, R. S. Yeats, and J. Ren (2013). Superquakes and supercycles, *Seismol. Res. Lett.* **84,** 24–32, doi: 10.1785/0220110135.

Goldfinger, C., L. D. Kulm, R. S. Yeats, B. Appelgate, M. MacKay, and G. F. Moore (1992). Transverse structural trends along the Oregon convergent margin: Implications for Cascadia earthquake potential, *Geology* **20,** 141–144.

Goldfinger, C., L D. Kulm, R. S. Yeats, L. C. McNeill, and C. Hummon (1997). Oblique strike-slip faulting of the central Cascadia submarine forearc, *J. Geophys. Res.* **102,** 8217–8243.

Goldfinger, C., A. E. Morey, B. Black, J. Beeson, C. H. Nelson, and J. Patton (2013). Spatially limited mud turbidites on the Cascadia margin: Segmented earthquake ruptures? *Nat. Hazards Earth Syst. Sci.* **13,** 2109–2146, doi: 10.5194/nhess-13-2109-2013.

Goldfinger, C., A. E. Morey, C. H. Nelson, J. Gutierrez-Pastor, J. E. Johnson, E. Karabanov, J. Chaytor, and A. Ericsson (2007). Rupture lengths and temporal history of significant earthquakes on the offshore and north coast segments of the northern San Andreas fault based on turbidite stratigraphy, *Earth Planet. Sci. Lett.* **254,** 9–27.

Goldfinger, C., C. H. Nelson, A. E. Morey, J. E. Johnson, J. R. Patton, E. Karabanov, J. Gutiérrez-Pastor, A. T. Eriksson, E. Gràcia, G. Dunhill, R. J. Enkin, A. Dallimore, and T. Vallier (2012). Turbidite event history—Methods and implications for Holocene paleoseismicity of the Cascadia subduction zone, *U.S. Geol. Surv. Profess. Pap. 1661-F*, 170 pp.

Gomberg, J., and Cascadia 2007, and Beyond Working Group (2010). Slow-slip phenomena in Cascadia from 2007 and beyond: A review, *GSA Bulletin* **122,** 963–978, doi: 10.1130/B30287.1.

Hanks, T. C., and H. Kanamori (1979). A moment magnitude scale, *J. Geophys. Res.* **84,** 2348–2350, doi: 10.1029/JB084iB05p02348.

Hayes, G. P., D. J. Wald, and R. L. Johnson (2012). Slab1.0: A three-dimensional model of global subduction zone geometries, *J. Geophys. Res.* **117,** no. B01302, doi: 10.1029/2011JB008524.

Holschneider, M., G. Zöller, and S. Hainzl (2011). Estimation of the maximum possible magnitude in the framework of a doubly truncated Gutenberg–Richter model, *Bull. Seismol. Soc. Am.* **101,** 1649–1659, doi: 10.1785/0120100289.

Hyndman, R. D., and K. Wang (1995). The rupture zone of Cascadia great earthquakes from current deformation and the thermal regime, *J. Geophys. Res.* **100,** 22,133–22,154.

Jackson, D. D., and M. Matsu'ura (1985). A Bayesian approach to nonlinear inversion, *J. Geophys. Res.* **90,** 581–591.

Kagan, Y. Y. (1997). Seismic moment-frequency relation for shallow earthquakes: Regional comparison, *J. Geophys. Res.* **102,** 2835–2852.

Kagan, Y. Y. (1999). Universality of the seismic moment-frequency relation, *Pure Appl. Geophys.* **155,** 537–573.

Kagan, Y. Y. (2002a). Seismic moment distribution revisited: I. Statistical results, *Geophys. J. Int.* **148,** no. 3, 520–541.

Kagan, Y. Y. (2002b). Seismic moment distribution revisited: II. Moment conservation principle, *Geophys. J. Int.* **149,** no. 3, 731–754.

Kagan, Y. Y. (2002c). Aftershock zone scaling, *Bull. Seismol. Soc. Am.* **92,** 641–655.

Kagan, Y. Y., and D. D. Jackson (2012). Whole Earth high-resolution earthquake forecasts, *Geophys. J. Int.* **190,** no. 1, 677–686, doi: 10.1111/j.1365-246X.2012.05521.x.

Kagan, Y. Y., and D. D. Jackson (2013). Tohoku earthquake: A surprise? *Bull. Seismol. Soc. Am.* **103,** 1181–1194, doi: 10.1785/0120120110.

Kagan, Y. Y., and F. Schoenberg (2001). Estimation of the upper cutoff parameter for the tapered Pareto distribution, *J. Appl. Probab.* **38A,** 158–175.

Kanamori, H. (2006). Lessons from the 2004 Sumatra–Andaman earthquake, *Phil. Trans. Roy. Soc. A.* **364,** 1927–1945, doi: 10.1098/rsta.2006.1806.

Knopoff, L. (2000). The magnitude distribution of declustered earthquakes in southern California, *Proc. Natl. Acad. Sci. Unit. States. Am.* **97,** 11,880–11,884.

Kreemer, C., W. E. Holt, and A. J. Haines (2003). An integrated global model of present-day plate motions and plate boundary deformation, *Geophys. J. Int.* **154,** 8–34.

Mazzotti, S., H. Dragert, J. Henton, M. Schmidt, R. Hyndman, T. James, Y. Lu, and M. Craymer (2003). Current tectonics of northern Cascadia from a decade of GPS measurements, *J. Geophys. Res.* **108,** no. B12, doi: 10.1029/2003JB002653.

McCaffrey, R. (2008). Global frequency of magnitude 9 earthquakes, *Geology* **36,** 263–266.

McCaffrey, R., R. W. King, S. J. Payne, and M. Lancaster (2013). Active tectonics of northwestern US inferred from GPS-derived surface velocities, *J. Geophys. Res.* **118,** 709–723, doi: 10.1029/2012JB009473.

McCaffrey, R., M. D. Long, C. Goldfinger, P. Zwick, J. Nabelek, and C. Smith (2000). Rotation and plate locking at the southern Cascadia subduction zone, *Geophys. Res. Lett.* **27,** 3117–3120.

McCaffrey, R., A. I. Qamar, R. W. King, R. Wells, G. Khazaradze, C. A. Williams, C. W. Stevens, J. J. Vollick, and P. C. Zwick (2007). Fault locking, block rotation and crustal deformation in the Pacific northwest, *Geophys. J. Int.* **169,** 1,315–1,340, doi: 10.1111/j.1365-246X.2007.03371.x.

Minoura, K., F. Imamura, D. Sugawara, Y. Kono, and T. Iwashita (2001). The 869 Jogan tsunami deposit and recurrence interval of large-scale tsunami on the Pacific coast of northeast Japan, *J. Nat. Disast. Sci.* **23,** no. 2, 83–88.

Mitchell, C. E., P. Vincent, R. J. I. Weldon, and M. A. Richards (1994). Present-day vertical deformation of the Cascadia margin, Pacific northwest, U.S.A., *J. Geophys. Res.* **99,** 12,257–12,277.

Musson, R. M. W. (2000). Generalised seismic hazard maps for the Pannonian basin using probabilistic methods, *Pure Appl. Geophys.* **157,** nos. 1/2, 147–169.

National Earthquake Information Center (NEIC) (1970). Preliminary determination of epicenters monthly listing, *U.S. Department of the Interior*, 8 pp.

Nelson, A. R., H. M. Kelsey, and R. C. Witter (2006). Great earthquakes of variable magnitude at the Cascadia subduction zone, *Quaternary Res.* **65,** 354–365.

Oppenheimer, D., J. Eaton, A. Jayko, M. Lisowski, G. Marshall, M. Murray, R. Simpson, R. Stein, G. Beroza, and M. Magee et al. (1993). The Cape Mendocino, California, earthquakes of April, 1992: Subduction at the triple junction, *Science* **261,** 433–438.

Pacheco, J. F., L. R. Sykes, and C. H. Scholz (1993). Nature of seismic coupling along simple plate boundaries of the subduction type, *J. Geophys. Res.* **98,** no. B8, 14,133–14159, doi: 10.1029/93JB00349.

Petersen, M. D., A. D. Frankel, S. C. Harmsen, C. S. Mueller, K. M. Haller, R. L. Wheeler, R. L. Wesson, Y. Zeng, O. S. Boyd, D. M. Perkins, N. Luco, E. H. Field, C. J. Wills, and K. S. Rukstales (2008). Documentation for the 2008 Update of the United States National Seismic Hazard Maps, *U.S. Geol. Surv. Open-File Rept. 2008-1128*, 61 pp.

Pisarenko, V. F., and D. Sornette (2004). Statistical methods of parameter estimation for deterministically chaotic time series, *Phys. Rev. E* **69,**

036122, available at http://arXiv.org/abs/physics/0308059 (last accessed October 2013).

Pisarenko, V. F., A. Sornette, D. Sornette, and M. V. Rodkin (2008). New approach to the characterization of M_{max} and of the tail of the distribution of earthquake magnitudes, *Pure Appl. Geophys.* **165,** 847–888.

Priest, G. R., C. Goldfinger, K. Wang, R. C. Witter, Y. Zhang, and A. M. Baptista (2009). Confidence levels for tsunami-inundation limits in northern Oregon inferred from a 10,000-year history of great earthquakes at the Cascadia subduction zone, *Nat. Hazards* **54,** no. 1, 27–73, doi: 10.1007/s11069-009-9453-5.

Reiter, L. (1990). *Earthquake Hazard Analysis: Issues and Insights*, Columbia University Press, New York, New York, 254 pp.

Rong, Y., D. D. Jackson, and Y. Y. Kagan (2003). Seismic gaps and earthquakes, *J. Geophys. Res.* **108,** doi: 10.1029/2002JB002334.

Ruff, L., and H. Kanamori (1980). Seismicity and the subduction process, *Phys. Earth Planet. Int.* **23,** no. 3, 240–252, doi: 10.1016/0031-9201(80)90117-X.

Satake, K., K. Shimazaki, Y. Tsuji, and K. Ueda (1996). Time and size of a giant earthquake in Cascadia inferred from Japanese tsunami records of January, 1700, *Nature* **379,** 246–249.

Satake, K., K. Wang, and B. F. Atwater (2003). Fault slip and seismic moment of the 1700 Cascadia earthquake inferred from Japanese tsunami descriptions, *J. Geophys. Res.* **108,** no. B11, 2535, doi: 10.1029/2003JB002521.

Savage, J. C., and M. Lisowski (1991). Strain measurements and potential for a great subduction earthquake off the coast of Washington, *Science* **252,** 101–103.

Scholz, C. H., and J. Campos (2012). The seismic coupling of subduction zones revisited, *J. Geophys. Res.* **117,** no. B05310, doi: 10.1029/2011JB009003.

Schorlemmer, D., S. Wiemer, and M. Wyss (2005). Variations in earthquake-size distribution across different stress regimes, *Nature* **437,** doi: 10.1038/nature04094.

Schwartz, S. Y., and J. M. Rokosky (2007). Slow slip events and seismic tremor at circum-Pacific subduction zones, *Rev. Geophys.* **45,** doi: 10.1029/2006RG000208.

Secanell, R., D. Bertil, C. Martin, X. Goula, T. Susagna, M. Tapia, P. Dominique, D. Carbon, and J. Fleta (2008). Probabilistic seismic hazard assessment of the Pyrenean region, *J. Seismol.* **12,** 323–341.

Sipkin, S. A., W. J. Person, and B. W. Presgrave (2000). Earthquake bulletins and catalogs at the USGS National Earthquake Information Center, *IRIS Newsletter* **2000,** 2–4.

Stein, S., and E. Q. Okal (2011). The size of the 2011 Tohoku earthquake need not have been a surprise, *Eos Trans. AGU* **92,** no. 27, doi: 10.1029/2011EO270005.

Strasser, F. O., M. C. Arango, and J. J. Bommer (2010). Scaling of the source dimensions of interface and intraslab subduction-zone earthquakes with moment magnitude, *Seismol. Res. Lett.* **81,** no. 6, 941–950.

Sugawara, D., K. Goto, F. Imamura, H. Matsumoto, and K. Minoura (2012). Assessing the magnitude of the 869 Jogan tsunami using sedimentary deposits: Prediction and consequence of the 2011 Tohoku-oki, *Sediment. Geol.* 282**,** 14–26.

Utsu, T. (1999). Representation and analysis of the earthquake size distribution: A historical review and some new approaches, *Pure Appl. Geophys.* **155,** 509–535.

Vilanova, S. P., and J. F. B. D. Fonseca (2007). Probabilistic seismic-hazard assessment for Portugal, *Bull. Seismol. Soc. Am.* **97,** 1702–1717.

Wang, K., R. Wells, S. Mazzotti, R. D. Hyndman, and T. Sagiya (2003). A revised dislocation model of interseismic deformation of the Cascadia subduction zone, *J. Geophys. Res.* **108,** no. B1, 2026, doi: 10.1029/2001JB001227.

Wang, L., C. K. Shum, F. J. Simons, A. Tassara, K. Erkan, C. Jekeli, A. Braun, C. Kuo, H. Lee, and D. Yuan (2012). Coseismic slip of the 2010 M_w 8.8 great Maule, Chile, earthquake quantified by the inversion of grace observations, *Earth Planet. Sci. Lett.* **335,** 167–179.

Wech, A. G., K. C. Creager, and T. I. Melbourne (2009). Seismic and geodetic constraints on Cascadia slow-slip, *J. Geophys. Res.* **114,** no. B10316, doi: 10.1029/2008JB006090.

Witter, R. C., Y. Zhang, K. Wang, C. Goldfinger, G. R. Priest, and J. C. Allan (2012). Coseismic slip on the southern Cascadia megathrust implied by tsunami deposits in an Oregon lake and earthquake-triggered marine turbidites, *J. Geophys. Res.* **117,** no. B10303, doi: 10.1029/2012JB009404.

Yoshida, Y., H. Ueno, D. Muto, and A. Aoki (2011). Source process of the 2011 off the Pacific coast of Tohoku Earthquake with the combination of teleseismic and strong motion data, *Earth Planets Space* **63,** no. 7, 565–569.

Zöller, G. (2013). Convergence of the frequency–magnitude distribution of global earthquakes: Maybe in 200 years, *Geophys. Res. Lett.* **40,** 3873–3877, doi: 10.1002/grl.50779.

Zöller, G., M. Holschneider, and S. Hainzl (2013). The maximum earthquake magnitude in a time horizon: Theory and case studies, *Bull. Seismol. Soc. Am.* **101,** 860–875, doi: 10.1785/0120120013.

Center for Property Risk Solutions
FM Global Research Division
1151 Boston-Providence Highway
Norwood, Massachusetts 02062
(Y.R., H.M.)

Department of Earth and Space Sciences
University of California
Los Angeles, California 90095
(D.D.J.)

College of Earth, Ocean and Atmospheric Sciences
Oregon State University
Corvallis, Oregon 97331
(C.G.)

Manuscript received 7 November 2013;
Published Online 16 September 2014